

## ABSTRACT

Title of Document:

EXPERIMENTAL CHARACTERIZATION OF  
SLOT FILM COOLING FLOWS WITH  
MINIMALLY INTRUSIVE DIAGNOSTICS

Fernando Raffan, M.S. 2008

Directed By:

André Marshall, Ph.D.  
Associate Professor Fire Protection Engineering,  
Adjunct Faculty Aerospace Engineering

The performance of a propulsion system is directly proportional to its operating temperature; therefore, an optimum operation regime will undoubtedly generate intense thermal loads on system components. If the system is designed for reusability and/or long range missions, it may be necessary to perform active cooling of critical components to prevent premature failure of the system. One such method is film cooling, in which a layer of relatively cool gas is injected near the surface to be protected. This work describes the use of minimally intrusive diagnostics to characterize the kinematics, thermal dynamics and heat transfer of slot film cooling flows over a wide range of blowing ratios, generating a comprehensive database for detailed analysis, as well as for further use by model developers.

EXPERIMENTAL CHARACTERIZATION OF SLOT FILM COOLING FLOWS  
WITH MINIMALLY INTRUSIVE DIAGNOSTICS

By

Fernando Raffan

Thesis submitted to the Faculty of the Graduate School of the  
University of Maryland, College Park, in partial fulfillment  
of the requirements for the degree of

M.S in Aerospace  
Engineering  
2008

Advisory Committee:  
André Marshall, Ph.D., Chair  
Chris Cadou, Ph.D.  
Arnaud Trouvé, Ph.D.

© Copyright by  
Fernando Raffan  
2008

## Dedication

To God, my family, my girlfriend, my friends, and anyone else who ever believed in me.

## Acknowledgements

This work was performed under the NASA CUIP program, which provided the funding for this work. Thanks to Claudia Mayer, program manager, and Paul Tucker and Doug Westra, our NASA points of contact. I would also like to thank the committee members for the guidance and support throughout this research endeavor. My gratitude goes towards Dr. André Marshall and Dr. Chris Cadou, my co-advisers, who provided priceless insight into the problem at hand. Thanks to Mr. Kiran Dellimore, who has also been part of this project. Finally, special thanks go to my friend and colleague, Mr. Carlos Cruz, who worked hand in hand with me on this project and lent his expertise from previous film cooling investigations in developing this comprehensive experimental study.

# Table of Contents

Dedication.....	ii
Acknowledgements .....	iii
Table of Contents .....	iv
List of Tables .....	vi
List of Figures .....	vii
Nomenclature.....	ix
Chapter 1: Introduction.....	1
<u>1.1 Motivation</u> .....	2
<u>1.2 Background</u> .....	4
1.2.1 Scaling Laws.....	4
1.2.2 Influence of Turbulence Intensity.....	13
1.2.3 Geometry Effects .....	14
1.2.4 Diagnostics .....	14
<u>1.3 Objectives of the Current Work</u> .....	16
Chapter 2: Investigative Approach.....	18
<u>2.1 Experimental Facility Design</u> .....	18
<u>2.2 Diagnostics</u> .....	21
2.2.1 PIV .....	21
2.2.2 IR Thermography.....	27
2.2.3 Microthermocouples .....	29
<u>2.3 Investigative Methodology</u> .....	30
<u>2.4 Experimental Approach</u> .....	32
2.4.1 Heat Transfer Calculations.....	34
<u>2.5 Uncertainty Analysis</u> .....	39
2.5.1 PIV .....	39
2.5.2 Gas Temperatures (microthermocouples) .....	40
2.5.3 IR Thermography.....	41
2.5.4 Heat Transfer .....	42
Chapter 3: Results .....	44
<u>3.1 Basic Flow Characteristics (m=3.01)</u> .....	44
3.1.1 Flow Visualization .....	44
3.1.2 Kinematics.....	45
3.1.3 Thermal mixing dynamics.....	50
<u>3.2 Case comparison</u> .....	51
3.2.1 Pure Mixing .....	52
3.2.1.1 Flow Visualization .....	53
3.1.1.2 Kinematics .....	55
3.1.1.3 Thermal Mixing .....	57
3.1.2 Non-adiabatic boundary condition.....	58
Chapter 4: Conclusions.....	63
<u>4.1 Summary of results</u> .....	63
4.1.1 Adiabatic wall effectiveness .....	63

4.1.1 Flow visualization.....	64
4.1.2 Kinematics .....	64
4.1.3 Thermal mixing.....	65
4.1.4 Heat Transfer .....	65
<u>4.2 Suggestions for future research .....</u>	66
Appendix A. Kinematics .....	68
Appendix B. Thermal Mixing.....	75
Bibliography .....	77

## List of Tables

Table 1. UMD hot wind tunnel operating conditions.....	19
Table 2. Test matrix for the current work.....	31

## List of Figures

Figure 1. Film cooling of a rocket engine (adapted from Sutton <sup>1</sup> ) .....	2
Figure 2. Film cooling of an air breathing engine combustor .....	2
Figure 3. J2-X conceptual design (NASA).....	3
Figure 4. UMD Hot Wind Tunnel (adapted from Cruz and Marshall <sup>18</sup> ).....	18
Figure 5. Test section schematic .....	20
Figure 6. Assembled test section.....	22
Figure 7. Typical PIV system components and operation (adapted from Raffel <sup>39</sup> )....	23
Figure 8. Schematic of seeder operation for PIV .....	25
Figure 9. PIV setup in UMD Hot Wind Tunnel.....	26
Figure 10. IR camera setup .....	29
Figure 11. Microthermocouple probe (adapted from Cruz and Marshall <sup>18</sup> ).....	30
Figure 12. Inlet profile comparison between adiabatic and non-adiabatic wall-wake case. ....	33
Figure 13. Geometry for radiation configuration factor calculation (from Jakob <sup>45</sup> )...	37
Figure 14. Schematic of heat transfer to plate .....	38
Figure 15. Flow visualization for m = 3.0. a) Nearfield, 0 < x/s < 25, b) Farfield, ....	45
Figure 16. Near field contour map of velocity for m = 3.0. ....	46
Figure 17. Profiles of x-component of velocity, u, for m = 3.0.....	46
Figure 18. RMS profiles of 2-D components of velocity. a) $u_{rms}$ , b) $v_{rms}$ .....	47
Figure 19. Instantaneous velocity fluctuation vector fields, with $u'$ contour visualization criterion and $y_{1/2}$ location. a) 0 < x/s < 6, b) 0 < x/s < 12 .....	49
Figure 20. Closeup of roller structures highlighted in Figure 19.....	50
Figure 21. a) Raw temperature profiles for m = 3.0 case, b) RMS of temperature ....	51
Figure 22. Adiabatic wall effectiveness, $\eta_{aw}$ vs. x/s.....	52
Figure 23. Flow visualization for all cases. a) $m = 0.66$ , b) $m = 1.32$ , c) $m = 3.01$ .....	53
Figure 24. Turbulent structures due to shear. a) Clockwise roller for $VR < 1.0$ , b) no preference for $VR \sim 1.0$ , c) counterclockwise roller for $VR > 1.0$ .....	54
Figure 25. Inlet velocity profiles for all cases.....	55
Figure 26. Velocity profiles far downstream, $x/s \sim 47.2$ , for all cases.....	56
Figure 27. a) Inlet thermal profiles comparison, b) thermal profiles at $x/s = 34.5$ .....	57
Figure 28. Governing temperatures for heat transfer problem. ....	59
Figure 29. Conjugate heat transfer .....	60
Figure 30. Convective heat transfer coefficient, $h$ .....	61
Figure 31. $St_\infty$ vs. $Re_x$ .....	62

## Appendix Figures

Figure A. 1. a) - f) VR = 0.5 Near Field .....	69
Figure A. 2. a) - f) VR = 0.5 Far Field .....	70
Figure A. 3. a) - f) VR = 1.0 Near Field .....	71
Figure A. 4. a) - f) VR = 1.0 Far Field .....	72
Figure A. 5. a) - f) VR = 2.0 Near Field .....	73
Figure A. 6. a) - f) VR = 2.0 Far Field .....	74

Figure B. 1. Non-dimensional thermal profiles a) $m = 0.66$ adiabatic, b) $m = 0.66$ non-adiabatic, c) $m = 1.32$ adiabatic, d) $m = 1.32$ non-adiabatic, e) $m = 3.01$ adiabatic, f) $m = 3.01$ non-adiabatic.....	75
Figure B. 2. Non-dimensional thermal RMS profiles a) $m = 0.66$ adiabatic, b) $m = 0.66$ non-adiabatic, c) $m = 1.32$ adiabatic, d) $m = 1.32$ non-adiabatic, e) $m = 3.01$ adiabatic, f) $m = 3.01$ non-adiabatic.....	76

# Nomenclature

## Roman

$A$	area
$C_p$	specific heat at constant pressure
$c$	speed of light in a vacuum = 299,792,458 m/s
$dA$	differential area element
$d_{diff}$	diffraction limited particle diameter
$d_i$	particle image diameter
$d_p$	particle seeding diameter
$e$	Euler's constant $\sim 2.718$
$f\#$	f number of Particle Image Velocimetry optics
$F$	view factor for radiation calculations
$h$	convective heat transfer coefficient
$I$	turbulence intensity, radiation intensity
$k$	thermal conductivity
$l$	length
$m$	blowing ratio
$M$	magnification of Particle Image Velocimetry optics
$q''$	heat flux
$Re$	Reynolds' number
$s$	slot height
$t$	wall thickness
$T$	temperature
$TR$	temperature ratio
$U, u$	x-component of velocity
$V, v$	y-component of velocity
$VR$	velocity ratio
$x$	longitudinal coordinate, downstream of injection location
$y$	wall-normal coordinate

## Greek

$\delta_T$	thermal thickness
$\epsilon$	thermal emissivity
$\eta$	effectiveness
$\kappa$	Boltzmann's constant = $1.3806504 \times 10^{-23} \text{ J/K}$
$\lambda$	wavelength
$\nu$	kinematic viscosity
$\pi$	$\Pi \sim 3.14159$
$\rho$	fluid density
$\tau$	time constant of thermocouple
$\Psi$	Planck's constant = $6.626070 \times 10^{-34} \text{ J}\cdot\text{s}$
$\sigma$	Stefan-Boltzmann constant = $5.6704 \times 10^{-8} \text{ W/m}^2\text{K}^4$

## Subscripts

$aw$	adiabatic wall
$b$	bead
$bw$	backside wall
$c$	coolant
$cond$	conduction
$conv$	convection
$gas$	gas measurement
$o$	casing
$po$	plate to casing
$pw$	plate to window
$rad$	radiation
$rms$	root mean square
$w$	wall
$\infty$	mainstream

## Chapter 1: Introduction

The performance of a propulsion system is directly proportional to its operating temperature; therefore, an optimum operation regime will undoubtedly generate intense thermal loads on system components (combustor walls, turbine blades, nozzle walls, etc.) If the system is designed for reusability and/or long range missions, it becomes imperative to perform active cooling of critical components to prevent premature failure of the system. Sutton<sup>1</sup> explains that a considerable amount of heat is transferred in all designs and operations of rockets, and it is the designer's principal objective to safely limit this transfer by limiting the temperatures of the materials in these critically hot regions. Hill and Peterson<sup>2</sup> also emphasize this concept and extend the analysis of cooling to air breathing engines as well.

One of the most common approaches to deal with heat transfer to system components in both air breathing engines and rockets is film cooling which is often combined with backside wall cooling. Depending on the type of system and nature of the component that is to be protected, slots or holes are used to inject the coolant flow into the mainstream. Figure 1 shows a general rocket film cooling scheme, while Figure 2 shows a general gas turbine combustor film cooling scheme. Regardless of the application, it is very important to understand the physical processes that govern the mixing mechanisms and the resulting heat transfer when film cooling is used as thermal protection.

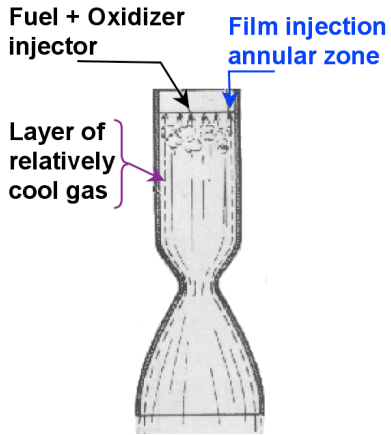


Figure 1. Film cooling of a rocket engine (adapted from Sutton<sup>1</sup>)

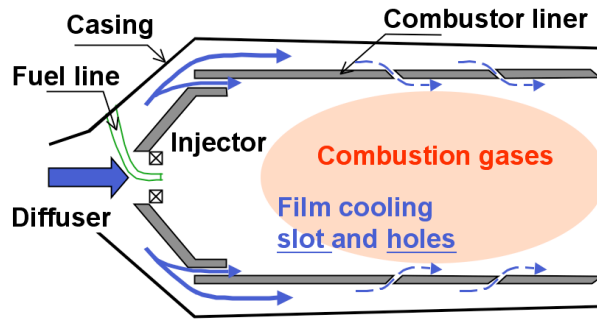


Figure 2. Film cooling of an air breathing engine combustor

### 1.1 Motivation

Recently, NASA's vision for exploration set forth a number of missions requiring a return to the moon and a manned trip to Mars. These missions require both reusable and long range propulsion systems, making them great candidates for film cooling. Plans for the J2-X engine, which will power NASA's vehicles for these missions, include using film cooling in the thrust chamber and nozzle extension. Figure 3 shows a preliminary schematic of the conceptual design for the J2-X.

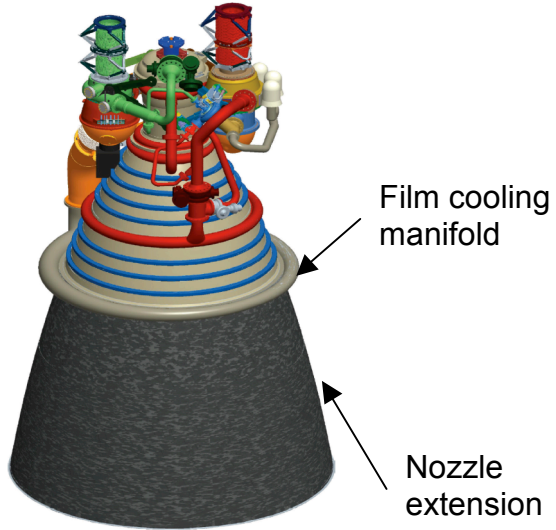


Figure 3. J2-X conceptual design (NASA)

Current design practice relies heavily on CFD modeling before building actual systems. However, this design approach requires reliable data for development and validation of the codes. Since film cooling flows involve complex kinematics and thermodynamics (boundary layers, shear layers, wall-jets, thermal mixing, heat transfer; all of which are coupled), the required data set must be comprehensive (include kinematics and thermodynamics) and correlated (i.e. obtained at the same conditions) for a proper validation. Unfortunately, most available film cooling data focuses on only one aspect of the problem; that is, one can find data for kinematics, thermal mixing or heat transfer independently, and so the coupled nature of the problem cannot be resolved. In support of NASA's efforts to meet the vision for exploration, this thesis describes a set of experimental tools that can be used to develop a comprehensive film cooling database suitable for model development and validation, as well as gaining further insight into the governing physics of film cooling.

## **1.2 Background**

Film cooling has undergone a significant evolution over the last 60 years. Early work was aimed mostly at determining the key parameters that govern film cooling performance, and developing semi-empirical scaling laws for the adiabatic effectiveness,  $\eta_{aw}$ , based on these parameters. Later, as diagnostics evolved, techniques such as Laser Doppler Anemometry (LDA), Particle Image Velocimetry (PIV) and Infrared (IR) Thermography were applied to gather global kinematic and thermal measurements. Results from these measurements provided new insight such as kinematics, turbulence intensities, and convective heat transfer coefficient distributions on the test wall. In the next paragraphs, a survey of the open literature dealing with film cooling will be presented, along with the most relevant findings.

### **1.2.1 Scaling Laws**

In 1946, Weighardt<sup>3</sup> performed one of the first experimental investigations in a film cooling type of flow. Although his original application consisted of injecting warm air tangentially through a slot as a means for deicing, the underlying physics are very similar to those governing film cooling. Weighardt examined the entrainment of the film by the mainstream, and varied the blowing ratio,  $m$ , and the injection angle. He then suggested a similarity expression for the flow temperature profiles by normalizing the results based on the local adiabatic wall temperature,  $T_{aw}$ , and the local thermal layer thickness,  $\delta_T$ . Another semi-empirical relation presented by Weighardt related the local adiabatic wall temperature to the slot geometry and flow parameters

(velocities, temperatures and densities). In 1953, Tribus and Klein<sup>4</sup> investigated heat transfer in boundary layers produced by jets of air discharged parallel to the surface. They first derived an analytical expression for the non dimensional wall temperature, defined as the adiabatic wall effectiveness

$$\eta_{aw} = \frac{T_\infty - T_{aw}}{T_\infty - T_c} \quad (1.1)$$

where  $T_\infty$ ,  $T_{aw}$  and  $T_c$  are the mainstream, adiabatic wall and coolant temperatures respectively.

In general terms, the merit of a film cooling scheme is determined by how  $\eta_{aw}$  behaves with downstream distance,  $x$ . Low values of  $\eta_{aw}$  indicate that the wall temperature is approaching the temperature of the hot mainstream, and signals the decay of the film. Thus, obtaining expressions for  $\eta_{aw}(x)$  will aid in the prediction of film decay and the lengthscale of the protection.

Tribus and Klein's expression was of the form

$$\eta_{aw}(x) = C_1 \text{Re}_s^{0.2} \left( \frac{x}{ms} \right)^{-0.8} \quad (1.2)$$

where

$$m = \frac{\rho_c U_c}{\rho_\infty U_\infty} \quad (1.3)$$

is the “blowing ratio”. Equation (1.2) shows that  $\eta_{aw}(x)$  depends on several inlet parameters, namely the slot Reynolds number ( $Re_s$ ), mainstream and coolant densities, ( $\rho_\infty$  and  $\rho_c$ ), slot height ( $s$ ), mainstream and coolant velocities ( $U_\infty$  and  $U_c$ ) and mainstream and coolant temperatures ( $T_\infty$  and  $T_c$ ). Tribus and Klein's result suggested

that  $Re_s$  is an important governing parameter in this type of flow, along with the relevant velocities, temperatures and densities.

By 1959, NASA was taking interest in film cooling technology. At NASA Lewis, Papell and Trout<sup>5</sup> investigated the usefulness and limitations of the technology. To do so, they extended Weighardt's experimental analysis from Weighardt by incorporating a wider range of parameters. The effect of each parameter was investigated systematically by varying it, while fixing all others. By doing so, it was observed that the effectiveness,  $\eta_{aw}$ , vs. non-dimensional downstream distance,  $x/s$ , was not particularly sensitive to slot height or freestream Mach number. However, it was sensitive to the blowing ratio, the temperature ratio and to some extent, the coolant temperature. Since the experimental parameters in this new analysis were well beyond the range of velocities and temperatures investigated at that time, Papell and Trout also attempted to correlate the data by modifying the general form of Weighardt's formula. Because of the wide range of parameters, a universal correlation could not be found. Instead, four separate correlations were presented, each one valid over a certain range of parameters.

Later in 1959, Hatch and Papell<sup>6</sup> presented an analytical model to predict the adiabatic wall temperature in a film cooled environment. To do so, they assumed that the film exists as a discrete thin layer, where there is no mixing between the coolant and the flow. Based on this rather gross assumption, the authors arrived at the general expression given by

$$\eta_{aw} = \exp\left(-\frac{hL(x - x')}{(\dot{m}c_p)_c}\right) \quad (1.4)$$

where  $h$  is the convective heat transfer coefficient,  $L$  is the slot width in the spanwise direction,  $x$  is the distance downstream of the injection point,  $x'$  is the characteristic length scale over which the adiabatic wall temperature does not rise,  $\dot{m}$  is the coolant massflow, and  $c_p$  is the specific heat of the coolant.

In 1960, Papell<sup>7</sup> extended the analysis from this model to angled slots and normal holes as injection methods for the coolant. Once again, his approach was to modify the original correlation to include the effects of the injection angle and then fit the data from the modified injection scheme to the equation. For angled slots, the new parameter was the effective slot injection angle, given as the angle of the fluid exiting the slot relative to the mainstream direction. For hole injection, an effective slot height,  $s'$ , was obtained by relating the massflow through an actual slot to that through the holes, was used. The data showed that any deviation from tangential injection usually results in decreased effectiveness. This result can be explained by the increased mixing due to the angularity between the streams inducing a higher level of mixing, which tends to “destroy” the film much sooner than in the tangential injection case.

In 1961, Welsh<sup>8</sup> reviewed the results of an earlier test run performed by Wilson and Boden at JPL. This review presented data obtained from an actual film cooled rocket engine. Because of this, only heat transfer measurements were presented, since obtaining velocity and temperature profiles would have been impossible in a live

engine firing. Interestingly, Welsh also presented the effect of film cooling on specific impulse reduction. This tradeoff between cooling the engine's components and having a performance reduction had not been previously investigated since most research to date had been performed under laboratory conditions, as opposed to using a real engine.

In Welsh's work, the effect of varying the film's massflow, chemical composition and coolant injector design on the heat transfer was examined. Coolant was injected at several stations throughout the thrust chamber and nozzle while a calorimeter setup was used to determine the heat transfer to the walls. Local heat transfer reduction was greatest for injection directly upstream of the nozzle. Using a deflector plate in the injector to redirect coolant flow tangentially to the wall offered a greater coolant effectiveness. Of all coolants, water performed the best, although the difference in heat transfer reduction among coolants in general was on the order of 20% upstream of the throat and 5% downstream. It should be noted that this experiment used liquid coolant, which must undergo a phase change as it flows downstream. As such, the traditional approach to predict film cooling performance must be modified significantly to account for the two-phase and transition type of flow.

Hartnett et al.<sup>9</sup> built on Weighardt's and Tribus and Klein's work by performing velocity measurements in addition to obtaining thermal and heat transfer characteristics. This is perhaps one of the few comprehensive analyses found in the literature, although it is restricted to a single slot size and a single blowing ratio. The authors replicated Weighardt's slot configuration, but added a heat transfer plate

which was fitted with an array of heaters to actively control the boundary conditions.

Velocity profiles were obtained with small pitot probes while flow thermal profiles were obtained with thermocouple probes.

Two distinct experiments were performed to characterize the test section in general, and two other experiments dealt directly with film cooling. First, a solid flat plate experiment was run to obtain turbulent boundary layer velocity profiles in the wind tunnel. Once these profiles were obtained, the authors were able to obtain the virtual origin of the boundary layer. In this same experiment, heat transfer to a plate with unheated starting length was also investigated and compared to theory, thereby validating the use of the heat transfer plate for future studies. Next, an isothermal experiment with film injection was performed in order to investigate the modified boundary layer profiles and to characterize the velocity profile inside the slot. Then, the authors performed adiabatic wall experiments with heated air injection. When compared to isothermal flow results, no significant effect from the heated film injection was found on the velocity profiles. Temperature profiles showed the expected variation in slope as one moves downstream and when non-dimensionalized using Weighardt's original analysis the profiled collapsed on each other.

However, plots of  $\eta_{aw}$  vs.  $x/ms$ , and comparison with previous data from other authors showed a 40% scatter in the data which the author's could not explain definitively. Finally, the constant heat input experiments allowed the Stanton number as a function of downstream distance,  $St(x)$ , to be determined and compared to the prediction from solid flat plate theory, showing good agreement. Thus, at least for this

configuration, the heat transfer coefficient may be determined directly from a Stanton number correlation, or calculated directly from the known local values of  $q''$ ,  $T_w$  and  $T_{aw}$  in the experiment.

In 1961, Seban and Back<sup>10</sup> performed an analysis on a wall-jet scenario, where the coolant injection velocity is much greater than that of the mainstream. The authors obtained velocity profiles experimentally, and proceeded to compare them with classical wall-jet theory, with good agreement (on the order of 2% error). Turbulent boundary layer theory was also used to obtain shear coefficients from the law of the wall. For temperature profiles, the agreement is relatively good (~2%-7% error depending on the location), but is achieved only by modifying the eddy viscosity term in the theoretical expression. Finally, heat transfer was also measured experimentally and compared to theory via the Colburn analogy, which relates the Stanton number to the Prandtl number and the friction coefficients. This comparison showed about 10% underprediction of heat transfer to the wall.

Later, Stollery and El-Ehwany<sup>11,12</sup> derived a correlation for film cooling, based on a boundary-layer model. The authors postulated that film cooling flows can be broken down into 3 separate regions: a potential core where the wall temperature is very close to that of the coolant, a second region resembling a wall-jet (in the case  $U_c > U_\infty$ ) otherwise, this region does not exist, and finally a third region where the flow resembles a turbulent boundary layer. The existence of the second region is governed by having a high momentum coolant relative to the mainstream, and is different from a true wall jet due to the non-zero mainstream velocity.

Seban and Back's approach was to rederive an analytical expression for the wall temperature in the boundary layer zone. Following Wieghardt's initial analysis, as well as building on the work by Hartnett et al. and Tribus and Klein, they arrived at the same expression for the effectiveness given in Eq. (1.2). Next, they used an enthalpy balance approach and also arrived to a very similar expression. However, the steps used in this new enthalpy balance approach allow for an easy extension of the correlation to include the cases of foreign gas injection (i.e. where coolant composition is different from that of the mainstream) and large density ratios. Comparing this new expression to those of previous researchers, the authors realized that they all have the same form as Eq. (1.2), except for the values of the leading coefficient  $C_1$ , which seemed to vary. They attributed this to the assumed form of the temperature profile in the derivation, since each author seemed to prefer a different form for it (exponential, 1/7 power law, etc.). Finally, the authors compared their expression to experimental data and showed that the rather large scatter in Hartnett et al.'s data can be explained by including the effect of  $Re_s$ , much like Tribus and Klein did in their work. When this effect is included, the scatter is reduced, and data from Tribus and Klein, Weighardt and Hartnett collapsed on a single curve.

Defining the velocity ratio, VR as

$$VR = \frac{U_\infty}{U_c} \quad (1.5)$$

the authors concluded that their expression was valid only for  $VR < 1.5$ , otherwise the flow could no longer be considered a boundary layer and a wall-jet treatment should be used instead.

Goldstein<sup>13</sup> performed a comprehensive review of available film cooling literature up to 1971. His analysis dealt with both slot and hole injection film cooling and included a summary of theoretical approaches and a summary of experimental results. A very useful summary of the reviewed geometries and parameter ranges was also presented. The author described the evolution of film cooling research with time, as well as the different approaches taken to develop proper scaling laws. Since most models are semi-empirical in nature, Goldstein pointed out that they should be used carefully, and that, in general, they are only valid far away from the injection point. These observations suggested a need for near-injection region data.

In 1973, Ballal and Lefebvre<sup>14</sup> expanded the analysis by Stollery and El-Ehwany to improve its accuracy in the near slot region. Stollery and El-Ehwany required solving for a modified energy equation invoking the Reynolds analogy and using a correlation to obtain the necessary skin friction coefficients. In this new approach, Ballal and Lefebvre suggested that the use of a correlation was not valid and skin friction coefficients should be obtained experimentally in this region. By doing so, and substituting their values into Stollery and El-Ehwany's analysis, the authors provided a new expression which was shown to agree within 5% of all of the data reviewed by Goldstein. It was valid for  $0 < x/s < 150$  which made it useful in the near slot region. However, it was not valid for large blowing ratios due to the assumptions in the velocity profile. To extend the analysis, the authors employed a wall-jet model to

derive a new expression for the effectiveness. This expression was, in turn, broken into two separate expressions, due to the fact that at  $x/ms > 11$  the flow tended to resemble a turbulent boundary layer. The wall-jet analysis extension, thus, provided two correlations, namely

$$\eta_{aw} = \left[ 0.6 + 0.05 \left( \frac{x}{ms} \right) \right]^{-1}, \quad x/ms < 11 \quad (1.6)$$

$$\eta_{aw} = 0.7 \left( \frac{x}{s} \right)^{-0.3} \text{Re}_s^{0.15} m^{-0.2}, \quad x/ms > 11 \quad (1.7)$$

Both expressions are valid for blowing ratios in the range  $1.3 < m < 4.0$ . Although the authors do not make it clear, these correlations are not necessarily continuous at  $x/ms = 11$

### 1.2.2 Influence of Turbulence Intensity

In 1986, Simon<sup>15</sup> at NASA built on the findings by Marek and Tacina<sup>16</sup> who suggested that turbulence intensities in the flow were also important parameters. Since film cooling is a mixing dominated flow, the turbulence intensities should have a significant effect on controlling the mixing strength, thus affecting the performance of the film cooling system. Simon developed a semi-empirical model by using Marek and Tacina's data, combining it with classic wall-jet theory by Abramovich<sup>17</sup> and including the effects of wall normal turbulence intensities in both the freestream and the slot,  $I_v$ , and  $I_{v,s}$  respectively. This model was used by Cruz and Marshall<sup>18</sup> as a basis for comparison to their experimental data, with good agreement (within 5%) in the near slot region.

Bons et al.<sup>19</sup> also investigated the effects of high freestream turbulence in film cooling. The geometry was that of a single row of holes, and freestream turbulence was generated by jets in crossflow. The idea was to replicate turbulent structures commonly found at the exit of gas turbine combustors. An elaborate experimental setup including instrumentation to obtain temperature and velocity profiles was used. It was shown that for hole-injection film cooling, the effects of freestream turbulence depend on hole arrangement geometry and blowing ratio. Therefore, it is important to quantify turbulence intensities in the freestream when performing film cooling experiments.

### 1.2.3 Geometry Effects

Taslim, et al.<sup>20</sup> investigated the effects of slot geometry on film cooling effectiveness. Their parametric study showed that  $\eta_{aw}$  is rather insensitive to the slot width to height ratio, moderately sensitive to the slot angle relative to freestream,  $\theta$ , for the range  $0^\circ < \theta < 15^\circ$ , and highly sensitive to the lip thickness to slot height ratios,  $t/s$ , in the range  $0.5 < t/s < 1.25$ . A similar parametric study was done at NASA by Burd and Simon<sup>21</sup>, aimed at characterizing hole injection.

### 1.2.4 Diagnostics

As minimally intrusive diagnostics became easier to implement, they were subsequently applied to characterize film cooling flows. Gogineni et al.<sup>22</sup> used PIV to measure the 2D velocity flowfield and turbulence intensities in the same experimental facility of Bons et al. A qualitative analysis of the results obtained from a seeded

coolant jet showed that for blowing ratios  $m < 1.0$ , increases in turbulence intensities significantly increase the spread of the coolant jet emanating from the holes. Sousa et al.<sup>23</sup> used a PIV system to visualize the near-wall region of a turbulent boundary layer. They obtained velocity profiles and turbulence statistics that matched the classical law of the wall results from turbulent boundary layer theory<sup>24</sup> within 2% and Direct Numerical Simulations from Spalart<sup>25</sup> within 2%. The authors also suggested sampling a large number of images over a statistically significant amount of time (i.e., much larger than the timescales of the flow), in order to improve the accuracy of the turbulence statistics.

Fukushima et al.<sup>26</sup> also used PIV and Planar Laser-Induced Fluorescence (PLIF) to investigate the mixing process in an axysymmetric turbulent jet. Their results were in excellent agreement with DNS investigations as both experimental and numerical profiles collapsed on each other. Peterson<sup>27</sup> also used the PIV technique to visualize structural features of jets in crossflow for film cooling applications. This detailed study showed the enormous potential of PIV as a useful tool for characterizing film cooling flows. Peterson was able to obtain instantaneous flow structures inside a single film cooling hole and track their evolution downstream of the injection point. Polanka et al.<sup>28</sup> used stereoscopic PIV to obtain the 3 velocity components near the stagnation region of a turbine blade with film cooling. The PIV system successfully obtained velocities in such a complex flow and the authors emphasized that the results can be of great value to CFD model development. For a more detailed explanation of the PIV technique and its direct application to turbulent mixing flow measurements,

the reader is referred to Kaehler<sup>29</sup>.

Infrared (IR) thermography has proved to be a very useful technique to determine the wall temperature. Simultaneous measurement of about 320 x 280 wall temperature points is possible, with an adjustable spatial resolution depending on the optical configuration of the system. Baldauf, Schulz, and Wittig<sup>30,31</sup> have several papers detailing the use of IR thermography to determine the temperature distribution over a film cooled plate using hole injection. The test plate included internal water cooling channels that permit heat transfer calculations. To do so, the authors used the measured temperatures and a Finite Element Analysis model of the plate to obtain local heat transfer values. The superposition principle, which consists of making 2 or more surface temperature measurements at distinct boundary conditions, was used to calculate the heat transfer coefficient. Full details of the procedure can be found in Saumweber et al.<sup>32</sup>, and further applications of the technique can be found in Schulz<sup>33</sup>. These investigations show that IR thermography is a very helpful technique that allows the extension of surface temperature measurements into heat transfer and convective heat transfer coefficient calculations with high spatial resolution.

### **1.3 Objectives of the Current Work**

As seen in the literature survey, a great amount of work has focused on developing scaling laws to determine film cooling effectiveness. New diagnostics have enabled global kinematic and thermal measurements that provide more insight into the underlying physics of film cooling flows. However, most investigations focus only on

one aspect at a time, be it kinematics, surface temperatures, heat transfer, or flow thermodynamics. In addition, most of the recent work has focused solely on hole injection film cooling. As an example, an investigation of hole injection film cooling using numerical results and sets of in-house experiments were performed at Clemson University<sup>34,35,36,37</sup>. However, these simulations were only aimed at obtaining adiabatic wall effectiveness and heat transfer results, and full kinematics or flow thermal analysis was not reported in either the computational or experimental results. Film cooling applications such as combustor liners, turbine blade trailing edges, and rocket thrust chambers and nozzles would benefit from research performed in a slot configuration. A comprehensive experimental approach will provide further insight by coupling global kinematic measurements to global and local thermal measurements and local heat transfer. It will also provide a great tool for model developers. Given the motivations discussed earlier, and in order to contribute to the current field of film cooling research, this work aims to:

- Use minimally intrusive diagnostics to obtain coupled kinematic flow measurements, thermal flow measurements, wall temperature measurements, and heat transfer measurements in a slot film cooling configuration.
- Implement the approach over a wide range of blowing ratios, particularly covering both wall-wake ( $VR < 1.0$ ) and wall-jet ( $VR > 1.0$ ) flow types.
- Establish a database of the results for further analysis both to provide better understanding of the underlying physics, and to assist model developers with validation.

## Chapter 2: Investigative Approach

The experimental approach will be discussed in this section. The experimental facility will be described along with the implemented diagnostics and operating principles. Relevant data post processing schemes and techniques will also be discussed.

### **2.1 Experimental Facility Design**

The backbone of this experimental investigation is the hot wind tunnel built by Cruz and Marshall<sup>18</sup> to perform film cooling experiments. It consists of a centrifugal fan, an inline methane burner to raise the freestream temperature, a contraction section, a test section and a diffuser and exhaust system. Figure 4 shows the details of the wind tunnel, while Table 1 summarizes the main flow parameters achievable in the wind tunnel. For more detailed information on the wind tunnel, the reader is referred to Cruz and Marshall<sup>18,38</sup>.

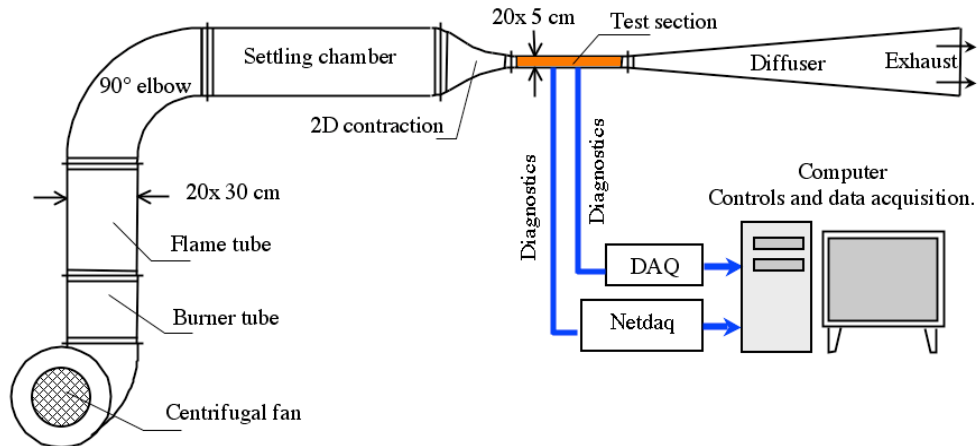


Figure 4. UMD Hot Wind Tunnel (adapted from Cruz and Marshall<sup>18</sup>)

	Quantities	Experimental Values	Remarks
Operating Conditions	$U_\infty$ $U_c$ $T_\infty$ $T_c$ $T_{bw}$	up to 40 m/s up to 50 m/s 300 - 500 K $\approx 300\text{K}$ $\approx 285\text{K}$	Mainstream velocity Cooling Film injection velocity Mainstream temperature Cooling film temperature Backside cooling temperature
Dimensionless Parameters	$Re_s$ $VR$ $TR$ $m$	2000 – 8000 0 - 3 1 - 2 0 - 6	Transitional - Turbulent film flow $VR = U_c / U_\infty$ $TR = T_\infty / T_c$ $m \approx VR \times TR$

Table 1. UMD hot wind tunnel operating conditions

### 2.1.1 Test Section

Because the wind tunnel was originally built for adiabatic experiments and thermal measurements only, a new test section had to be designed and built to accomodate the objectives of this work. Since both adiabatic and non-adiabatic conditions were of intrest, the test plate had to be of relatively low thermal conductivity to provide a credible adiabatic condition and provide large measurable temperature differences across a small thickness in the non-adiabatic cases. Furthermore, since laser diagnostics were also implemented, an optically transmissive material in the visible spectrum could help minimize reflections at the wall. After an extensive material search, UDEL®, a high temperature thermoplastic was chosen as the wall material. The test section casing was modified to incorporate large windows for both IR

thermography and PIV. Because the IR camera is sensitive to radiation in the 8-9  $\mu\text{m}$  range, CaF<sub>2</sub> windows, which are optically transmissive in the 1-10  $\mu\text{m}$  range were installed. This material also has a high resistance to humidity, a problem that often affects IR tailored optics. The windows were mounted on separate frames for easy cleaning. However, this presented a potential for leaks, as the frames were flush with the test section, but did not form an airtight seal.

The film cooling slot consisted of a stainless steel louver attached to the test plate. The slot height,  $s$ , was fixed at 4 mm, while the louver thickness,  $t$ , was 0.76 mm. This resulted in a lip thickness to slot height ratio,  $t/s < 40$ , which minimizes lip thickness effects as suggested by Goldstein.<sup>13</sup> The film was generated using a plenum attached to the back of the test plate. A small row of holes was used to feed air from the plenum into the slot. The film was formed as the jets impinged, mixed, and flowed downstream. Figure 5 shows a schematic of the test section.

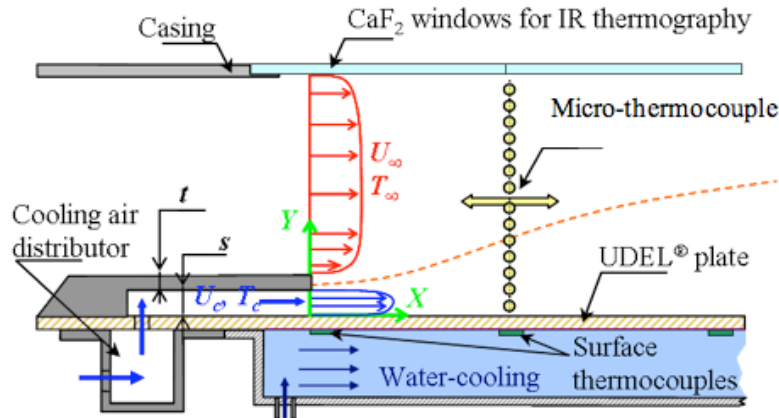


Figure 5. Test section schematic.

A water jacket was attached to the backside of the test plate for the non-adiabatic experiments. Four surface thermocouples were installed on the back of the test plate to monitor the wall temperature distribution on the water cooled side. For the adiabatic cases, the water jacket was removed, and an insulating board was attached to the backside of the test plate to further minimize heat loss. Figure 6 shows a photograph of the assembled test section.

## **2.2 Diagnostics**

The test section was instrumented with minimally intrusive diagnostics to minimize flow disturbances while obtaining comprehensive kinematic and thermal measurements. Particle Image Velocimetry (PIV) was chosen for kinematic measurements, with a possible future expansion using Laser Doppler Velocimetry (LDV). Infrared (IR) thermography was used to obtain wall temperature distributions on the film cooled side, while microthermocouple probes were used to obtain streamwise flow temperature profiles.

### **2.2.1 PIV**

PIV is a widely used technique for measuring the velocity flowfield in a plane. A typical PIV system consists of a pulsed laser, a camera, and a particle seeding system. The seeding system introduces particles into the flow whose sizes are carefully tailored to both follow the flow faithfully and scatter enough light to be detected by the camera.<sup>39</sup> The particles are illuminated by a planar laser sheet produced with a cylindrical lens.

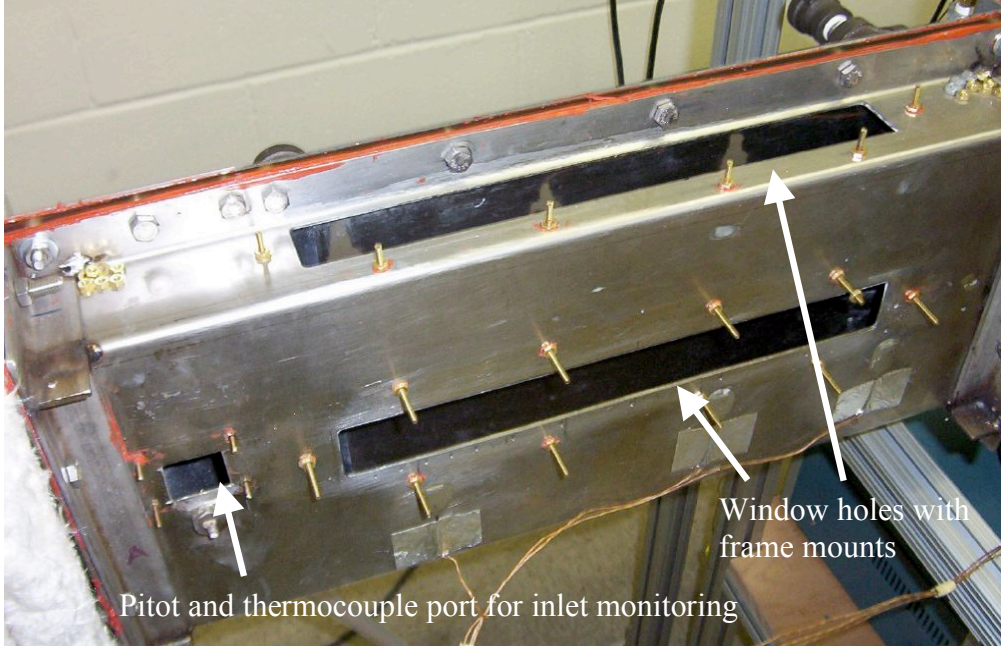


Figure 6. Assembled test section

The pulsed laser and the camera are synchronized such that two consecutive images are acquired. This effectively “freezes” a planar slice of the flow at two instants separated by the gate time,  $\Delta t$ . A cross-correlation algorithm is applied to obtain the net displacement vector of the particles at different points in the imaging area. The local velocities are then obtained by diving the net displacement by the known gate time. Figure 7 shows a schematic diagram of a typical PIV setup and operation.

To obtain reliable results, a particle’s image must be greater than a single pixel. In general, the diameter of a particle’s image on a CCD chip is given by:

$$d_i = \sqrt{(Md_p)^2 + d_{diff}^2} \quad (2.1)$$

where  $d_p$  is the physical diameter of the particle,  $M$  is the magnification of the optical system and  $d_{diff}$  is the so called diffraction limited image diameter given by:

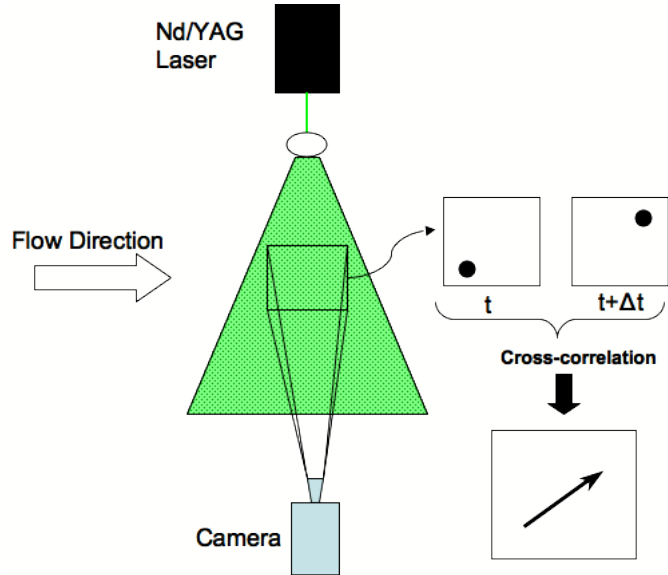


Figure 7. Typical PIV system components and operation (adapted from Raffel<sup>39</sup>)

$$d_{diff} = 2.44 f_{\#} (M + 1) \lambda \quad (2.2)$$

where  $f_{\#}$  is the f number of the lens system, and  $\lambda$  is the wavelength of the incident light on the particle. From these equations, it is evident that the image diameter of a particle differs from its physical diameter not only due to magnification, but also due to the scattered light's wavelength and lens setup. This allows for some control of the optimum particle image diameter without necessarily compromising the field of view, although tradeoffs are inevitable.

The seeding type, field of view, and gate time were selected in order to obtain the most reliable results.  $TiO_2$  was chosen as the seeding particle, since it is one of the few substances that can be introduced upstream of the in-line combustor without compromising its composition or physical state (as opposed to liquid droplets that may evaporate). Raffel<sup>39</sup> showed that PIV errors were minimized when  $d_i = 2$  pixels.

The green laser used in PIV corresponds to  $\lambda = 532$  nm, and  $\text{TiO}_2$  particles have a nominal diameter of 0.3-1.0  $\mu\text{m}$ . Based on this, a field of view of 5 cm x 5 cm, with a resulting magnification  $M = 0.3$  was chosen. The f-number of the lens was  $f_{\#} = 8$ , and average particle image diameters were on the order of 14  $\mu\text{m}$ , or  $\sim 2$  pixels. This field of view also resulted in a near wall resolution of  $\sim 0.25$  mm for the associated cross-correlation algorithm. A reduced field of view would increase the near wall resolution, but a larger amount of data and post-processing time would be needed to characterize the entire flowfield.

Two independent seeders were used to inject  $\text{TiO}_2$  particles into the mainstream and coolant stream respectively. They consisted of fluidized beds, made out of PVC pipes and brass sintered plates. High pressure air entered the seeders from the bottom, passed vertically upwards through the sintered plates and mixed with the  $\text{TiO}_2$  before leaving through the top. Mainstream seeding was introduced directly upstream of the combustor, while coolant seeding was mixed with coolant air upstream of the plenum. This injection setup was designed to maximize the residence time of the particles in the flow so that any disturbances arising from the seeding injection are smoothed out by the time the particles reach the test section. Figure 8 shows a schematic of the seeders and the flow pattern.

Another critical parameter was the choice of gate time,  $\Delta t$ . Because a PIV image is broken into interrogation regions during vector calculations, it is very important that a particle's image stays within the same interrogation region when the algorithm is applied. Typical interrogation window sizes are 32 pixels x 32 pixels, and so particle

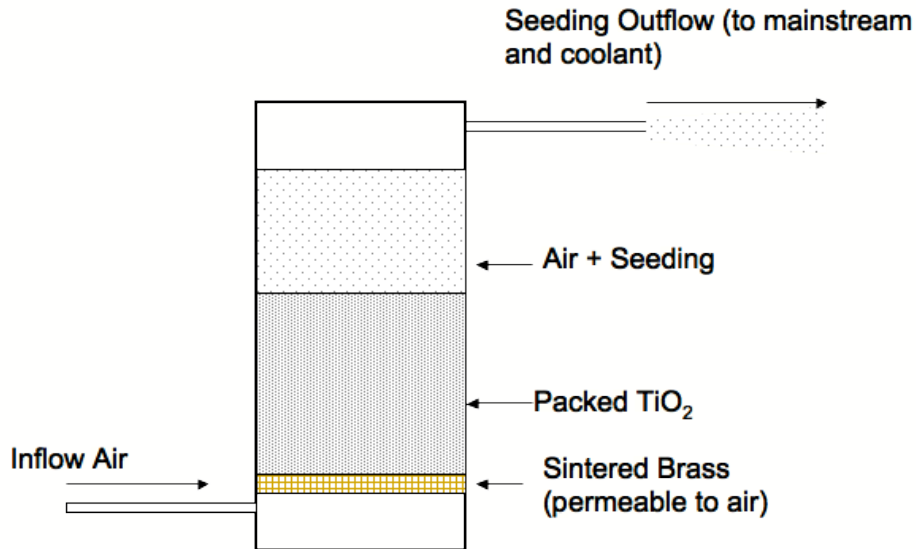


Figure 8. Schematic of seeder operation for PIV

displacement should be less than this characteristic size. In general, the PIV manufacturer recommends a particle displacement of 8-10 pixels in the region of highest velocities to obtain the most accurate results. Test runs were performed, and the algorithm applied to the test images. The  $\Delta t$  was gradually varied until this pixel displacement criteria was met, resulting in  $\Delta t = 8\mu\text{s}$  for all of the experiments performed in this work.

The wall was treated with a solution of Rhodamine 6G in white vinyl paint in order to minimize wall reflections and improve the signal to noise ratio in this region. When the light sheet comes in contact with the treated wall, the reflected energy is shifted to the fluorescent wavelength ( $\lambda = 566 \text{ nm}$ ) and blocked by a narrow 532 nm bandpass filter placed in front of the camera, substantially reducing noise from the wall reflections. A single camera Lavision PIV system was used in this work. It consisted of a 4 megapixel camera, a double cavity pulsed Nd/YAG laser and a processing computer.

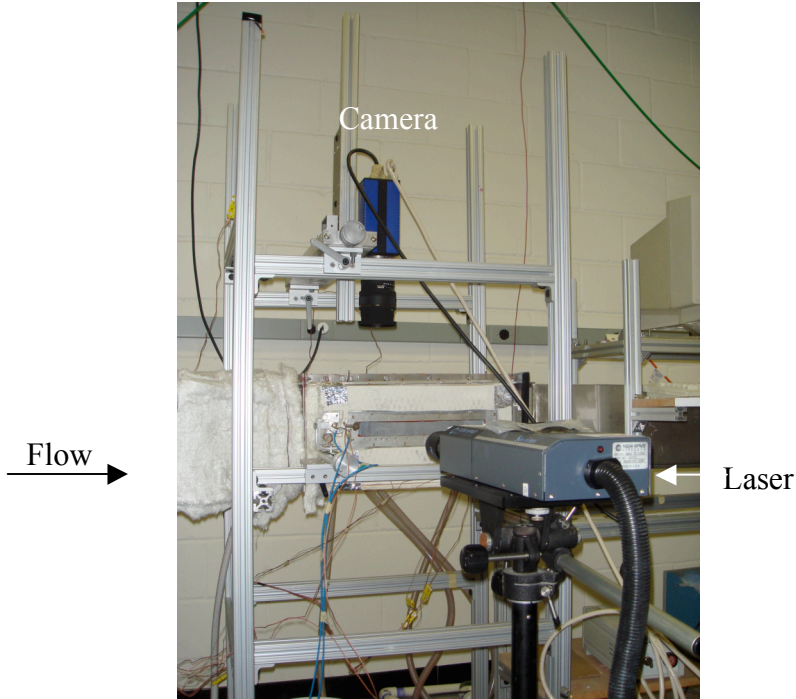


Figure 9. PIV setup in UMD Hot Wind Tunnel

A pitot tube in the mainstream and a massflow measurement for the slot provided reference velocities  $U_\infty$  and  $U_c$  respectively.

Per the suggestions of Sousa et al.<sup>23</sup> a total of 1000 image pairs were obtained at each downstream station in order to obtain statistically significant turbulence measurements. Four measurement stations were necessary to cover the entire length of the test plate resulting in a total of 4000 image pairs per experimental case. The images were post processed using a 32 x 32 pixel interrogation region with a 50% overlap using LaVision's DaVis software to obtain instantaneous and average vector maps of velocity and turbulence intensity. Images of a seeded coolant jet alone were also taken to provide flow visualization of mixing and jet growth. Figure 9 shows a picture of the PIV system setup in the wind tunnel. Works by Raffel et al.<sup>39</sup>, Westerweel<sup>40</sup> and Adrian<sup>41</sup> were used as guidelines for the setup and implementation

of the PIV system in this work.

### 2.2.2 IR Thermography

Global measurements of surface temperatures can be obtained using several techniques, including Temperature Sensitive Paint and Liquid Crystal Thermography. Both of these techniques require a special treatment of the surface to be measured, and require special laboratory illumination conditions and careful calibration. Instead, IR thermography was chosen due to its availability and relatively simple implementation in this particular film cooling configuration.

IR thermography works on the principle of detecting the infrared radiation emitted by a body<sup>42</sup>. According to Planck's law, this radiation is proportional to the body's temperature and is given by

$$I(\lambda) = \frac{2\pi\psi c^2}{\lambda^5(e^{\psi c/\lambda\kappa T} - 1)} \quad (2.3)$$

where  $\psi$  is Planck's constant,  $c$  is the speed of light in a vacuum,  $\kappa$  is the Boltzmann constant and  $\lambda$  is the wavelength associated with the radiant emittance of the body.

A typical infrared camera consists of a CMOS sensor able to detect the intensity of the emitted radiation in a particular and narrow wavelength band. Assuming perfect transmission of the radiation, and a perfect source with emissivity  $\epsilon = 1$ , Planck's law takes the form

$$I_{source} = \frac{A}{e^{B/T} + C} \quad (2.4)$$

where A,B, and C are constants built into the IR thermography software by the

manufacturer, and are generally based on the infrared wavelength range the camera is sensitive to and the camera's optical system. However, the hot mainstream flowing over the plate, the windows and the atmosphere also contribute to the actual signal detected by the camera. While one could theoretically correct for these effects, doing this accurately is cumbersome and difficult. To overcome this, Schulz<sup>33</sup> suggested an in-situ calibration using reference thermocouple measurements and Eq. (2.4). Given a number of thermocouple measurements and the raw signal from the camera, a non-linear least squares fitting method was applied to the data new values for A, B, and C, were obtained. These new values effectively account for all of the contributions to the signal and the true temperature can be obtained. Since a microthermocouple probe was used to obtain flow temperature profiles, the first measurement point of each profile, which corresponds to the probe being in direct contact with the wall, was used as the reference measurement for the IR calibration. A total of 5 wall temperature measurements were used to calibrate the IR images for each experiment. The fitting was accomplished using MATLAB's ® built in non-linear least squares fit algorithm, which is an implementation of the Levenberg-Marquardt method also used by Schulz<sup>33</sup>.

Wall temperature measurements were obtained with a FLIR Thermacam SC 3000 and Thermacam research software. A total of 30 images were obtained and averaged for each experiment. The analysis software was used to extract a representative measurement line of intensity data as a function of downstream distance. The calibration method was applied to recover the temperatures. Figure 10 shows a

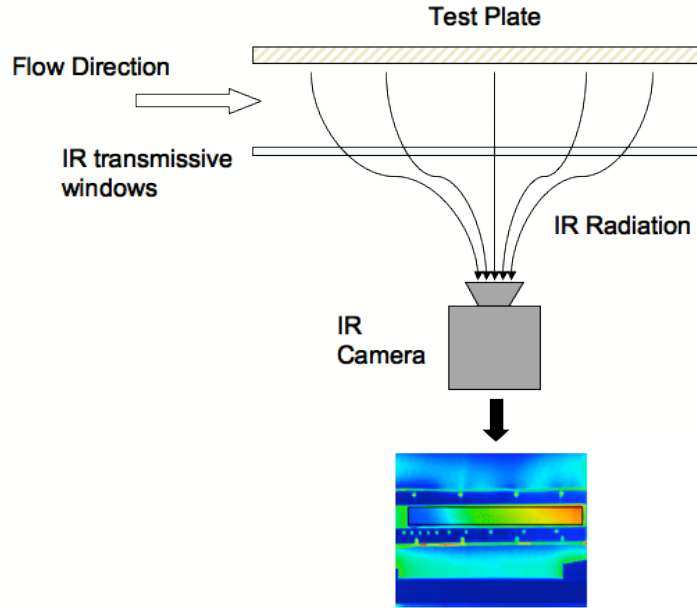


Figure 10. IR camera setup

schematic of the IR setup used in this work.

### 2.2.3 Microthermocouples

In order to obtain flow temperature profiles, it was necessary to obtain a fast response measurement with negligible contamination from radiation or other sources of error. It was also ideal to use a probe that would disturb the flow as little as possible. Microthermocouples were chosen because they meet these criteria. Probes were built using small diameter stainless steel tubes, a ceramic insert and a  $13\text{ }\mu\text{m}$  diameter wire K-type thermocouple bead protruding on one end. Figure 11 shows a detailed sketch of the probe. These probes were calibrated and connected to a National Instruments digital signal processing box. Labview® was used to sample data at 20 kHz.

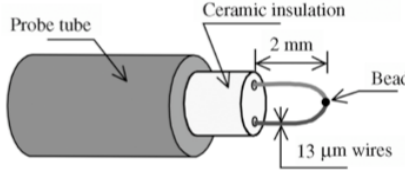


Figure 11. Microthermocouple probe (adapted from Cruz and Marshall<sup>18</sup>)

Data obtained using these microthermocouples had to be compensated for the thermal inertia of the bead. Following the method found in Cruz and Marshall<sup>18</sup>, the real gas temperature is given by

$$T_i = T_b + \tau \frac{dT_b}{dt} \quad (2.5)$$

where  $T_i$  is the actual gas temperature,  $T_b$  is the measured bead temperature, and  $\tau$  is the time constant of the bead. Values for the time constant were obtained by cycling the thermocouple through electrical heating-cooling cycles, while the derivative term was obtained through careful spectral analysis of the thermocouple signal. An algorithm developed by Cruz and Marshall was used to apply the digital compensation to obtain  $T_i$ , as well as to post process the data to obtain statistics such as mean temperature values, RMS, etc. Near wall resolution for thermal measurements was  $\sim 0.5$  mm.

### **2.3 Investigative Methodology**

The test matrix presented in Table 2 was created based on the findings from the literature survey and the requirements from the University of Maryland LES model developers. It covers a wide range of blowing ratios to make a clear distinction between wall-wake flow ( $VR < 1.0$ ), wall-jet flow ( $VR > 1.0$ ), and a limiting zero-shear

flow ( $VR \sim 1.0$ ). Because propulsion systems typically operate at the endpoints of the blowing ratio range, with rockets operating at low velocity ratios and gas turbines at high velocity ratios, this data is useful to develop film cooling in either propulsion system.

	<b>Case 1a</b>	<b>Case 1</b>	<b>Case 2a</b>	<b>Case 2</b>	<b>Case 3a</b>	<b>Case 3</b>
$U_\infty$ , m/s	24.86	24.86	22.10	22.10	11.00	11.00
$U_c$ , m/s	10.82	10.82	19.13	19.13	21.20	21.20
$VR$ ( $U_c/U_\infty$ )	0.44	0.44	0.87	0.87	1.93	1.93
$T_\infty$ , K	462.02	454.94	454.33	446.33	462.92	437.89
$T_c$ , K	304.78	306.11	298.88	304.43	296.33	301.54
$TR$ ( $T_\infty/T_c$ )	1.52	1.49	1.52	1.47	1.56	1.49
$m$ ( $VR \times TR$ )	0.66	0.65	1.32	1.27	3.01	2.80
$Re_s$	2651.75	2631.03	4856.63	4698.07	5466.11	5296.76

Table 2. Test matrix for the current work

Actual velocities were limited by the centrifugal fan. However, high values of  $Re_s$  were desired, not only since a turbulent coolant stream performs better, but also from a modeling standpoint, where turbulent inflow conditions must be established in order to obtain a valuable solution. Working hand in hand with Mr. Carlos Cruz, who was simultaneously developing an LES code for film cooling applications, a compromise was made in choosing satisfactory values of  $U_\infty$  and  $U_c$  such that the resulting experimental values of  $Re_s$  were suitable for use in simulations. Recalling the definition of blowing ratio from Eq. (1.3), and realizing that for this particular setup both the mainstream and coolant are essentially the same gas (air for the cooling flow and slightly vitiated air for the mainstream), one can invoke the ideal gas law to redefine the blowing ratio as

$$m = \frac{T_\infty U_c}{T_c U_\infty} \quad (2.6)$$

where it is assumed that the static pressure of both coolant and mainstream flows is identical. It should be noted that due to the detailed measurements and associated large amounts of data obtained in this work, the effects of temperature ratio,  $T_\infty/T_c$  (and therefore density ratio) variation were not studied and all cases exhibit identical temperature ratios. Instead, blowing ratio variations are solely due to variations in the velocity ratio.

As mentioned earlier in section (2.1.1), the lip thickness to slot height ratio was kept below the threshold for which lip effects have been reported to affect film cooling performance. In this sense, effects of geometry on film cooling physics are not studied in this work either. From a scaling law point of view, the effects of  $Re_s$ , blowing ratio,  $m$  (due to VR), and turbulence intensities  $I_u$ ,  $I_v$ , are the influential parameters relevant to this work.

#### **2.4 Experimental Approach**

For each blowing ratio investigated, two experiments were run; one with an adiabatic wall boundary condition and another non-adiabatic wall boundary condition with a cooled backside wall. Inflow conditions were kept as close as possible between adiabatic and non-adiabatic cases.

According to Hartnett<sup>9</sup>, kinematics are not influenced by the presence of a non-adiabatic boundary condition, provided that the velocities are similar compared to an adiabatic case. This was verified by performing PIV on a non-adiabatic reference case,

and comparing the results to those of an adiabatic case under the same reference inlet conditions. At the inlet, flow coolant velocities were matched, with a slight deviation in mainstream velocities of < 10%. It should be noted that this difference was due to slight variations in the reference pitot tube measurements and is not due to boundary conditions since these have no effect on inlet conditions. However, far downstream where boundary conditions may exert influence on velocity profiles, the initial discrepancy was maintained. This confirmed Hartnett's observation that boundary conditions do not affect the kinematics of the flow. Based on this, PIV was only run on adiabatic cases to optimize the workload and minimize collateral effects due to seeding contamination on laboratory equipment. IR thermography and flow profiles were performed in both cases.

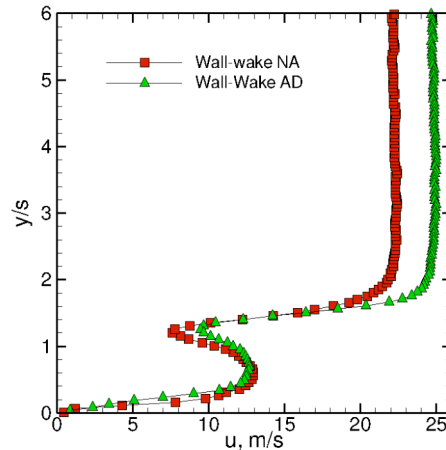


Figure 12. Inlet profile comparison between adiabatic and non-adiabatic wall-wake case.

Flow temperature data was used to obtain insight into the thermal mixing in both adiabatic and non-adiabatic cases. IR thermography was used to obtain the non-

adiabatic wall temperature,  $T_w$ , and the adiabatic wall temperature,  $T_{aw}$ . In the non-adiabatic experiments, the backside wall temperature,  $T_{bw}$  was monitored with 4 thermocouples. After reviewing the IR data, some non-physical oscillations in the raw IR signal were detected, suggesting possible contamination of the signal from seeding particles on the window. Furthermore, although the calibration method discussed in section (2.2.2) provides a good fit (IR temperatures and reference temperatures were within  $< 3\text{K}$  of each other), this error in wall temperatures can be significant in derived quantities. Because the values of the heat transfer,  $q''$ , and the convective heat transfer coefficient,  $h$ , are highly sensitive to the measured values of  $T_w$ , the IR data was not used in this work. Instead, microthermocouple measurements at the wall were used for the heat transfer analysis, since they provide more accurate measurements of  $T_w$ , at the expense of limited spatial resolution.

#### 2.4.1 Heat Transfer Calculations

Using wall temperature data from both adiabatic and non-adiabatic cases, film cooling heat transfer can be obtained. By placing the microthermocouple from the flow thermal measurements in contact with the wall, values for the non-adiabatic wall temperature,  $T_w$ , and adiabatic wall temperature,  $T_{aw}$ , were obtained.

In order to perform heat transfer analysis based on adiabatic vs. non-adiabatic measurements, one must ensure that the only difference between the cases is due to the boundary condition. However this is difficult to achieve in practice and some small deviations in the inlet conditions between non-adiabatic and adiabatic experiments were observed. Because of this, the measured value of  $T_{aw}$  was corrected

for use in heat transfer calculations, especially in obtaining the convective heat transfer coefficient.

The largest variations between cases occurred in the mainstream temperature while the coolant temperature exhibited smaller variations. In general, however, variations in slot Reynolds number and blowing ratio were not large, as indicated in Table 2. As seen in the scaling laws section of Chapter 1, the adiabatic wall effectiveness is a strong function of blowing ratio and slot Reynolds number. Because these quantities did not vary greatly between non-adiabatic and adiabatic cases despite the variations in inlet temperatures, one can assume that the adiabatic wall effectiveness,  $\eta_{aw}$ , obtained under the inlet conditions for the adiabatic case would not vary significantly from the adiabatic wall effectiveness associated with inlet conditions for the corresponding non-adiabatic case. Using the definition of adiabatic wall effectiveness, this assertion can be written as

$$\frac{T_{\infty,a} - T_{aw}}{T_{\infty,a} - T_{c,a}} = \frac{T_{\infty,na} - T_{aw,c}}{T_{\infty,na} - T_{c,na}} \quad (2.7)$$

where the left hand side is the adiabatic wall effectiveness evaluated at the adiabatic inlet conditions,  $T_{\infty,a}$ ,  $T_{c,a}$ , and the right hand side is the effectiveness evaluated at the non-adiabatic inlet conditions  $T_{\infty,na}$ ,  $T_{c,na}$ . To solve for the corrected adiabatic wall temperature,  $T_{aw,c}$ , one can rewrite Eq. (2.7) as

$$T_{aw,c} = T_{\infty} - \eta_{aw}(T_{\infty,na} - T_{c,na}) \quad (2.8)$$

yielding the corrected adiabatic wall temperature.

In the non-adiabatic experiments, the local conductive heat flux across the wall,  $q''_{cond}$ , can be readily obtained since both  $T_w$  and  $T_{bw}$  are directly measured and the thermal conductivity of the UDEL® plate and its thickness are known ( $k_w = 0.26$

W/mK and  $t_w = 6.35$  mm, respectively). Hence, using Fourier's law and assuming constant properties across the solid, the conductive heat flux per unit area across the wall is expressed by,

$$q''_{cond} = \frac{k_w}{t_w} (T_w - T_{bw}) \quad (2.9)$$

A heat transfer balance on the plate states that the net radiation to the wall added to the convection from the film to the wall must equal the conductive heat flux across the wall,

$$q''_{conv} + q''_{rad} = q''_{cond} \quad (2.10)$$

where the right hand side has been calculated from Eq. (2.9).

Initial data analysis showed that radiation effects were small compared to the total heat flux to the plate. To verify this, and properly account for it, radiation heat flux was calculated via the direct approach, found in Siegel and Howell<sup>43</sup>. This method assumes that the heat transfer occurs only between two surfaces, and none of the heat leaving one surface can be reflected back. A more accurate and involved method is the radiosity approach described by Modest<sup>44</sup>, but the improvement in accuracy is only a few percent.

For this particular setup, one can assume that there will be no net heat transfer between the window and the test plate, and that any heat transfer due to the presence of the thermally transparent window would be between the plate and the laboratory. Because the laboratory is at a much lower temperature than the casing, heat transfer between the plate and the laboratory is negligible when compared to heat transfer between the casing and the plate. Defining the configuration factor,  $F_{ij}$ , as the ratio of

the energy leaving surface  $i$  that reaches surface  $j$ ,  $F_{po}$  is the fraction of energy leaving the test plate that reaches the casing. To obtain  $F_{po}$ , one must first calculate the configuration factor between the plate and IR window,  $F_{pw}$ . Assuming that the wall temperature is measured on a small element of the test plate, with area  $dA$ , and the window is a rectangle in a plane parallel to  $dA$ , the configuration factor from the test plate element to the window,  $F_{pw}$  is given by Jacob<sup>45</sup> as

$$F_{pw} = \frac{1}{2\pi} \left( \frac{B}{\sqrt{1+B^2}} \sin^{-1} \frac{C}{\sqrt{1+B^2+C^2}} + \frac{C}{\sqrt{1+C^2}} \sin^{-1} \frac{B}{\sqrt{1+B^2+C^2}} \right) \quad (2.11)$$

where  $B$ , and  $C$  are the geometric parameters defined in Figure 13. In this figure,  $dA$  corresponds to the measurement point on the test plate and  $W$  corresponds to the relevant window area.

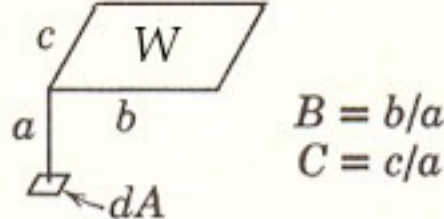


Figure 13. Geometry for radiation configuration factor calculation (from Jakob<sup>45</sup>)

It should be noted that this configuration factor changes depending on the relative location of the measurement point with respect to the window and, effectively,

$$F_{pw} = F_{dA-w}.$$

Because all of the energy leaving the test plate will reach either the casing or the surroundings through the thermally transparent window, this implies that

$$\begin{aligned} F_{po} + F_{pw} &= 1 \\ F_{po} &= 1 - F_{pw} \end{aligned} \quad (2.12)$$

The thermal emissivity of the stainless steel casing,  $\epsilon_o = 0.2$ , was found in Mills<sup>46</sup>, while the thermal emissivity of the UDEL® plate,  $\epsilon_w = 0.91$ , was assumed to be that of more common thermoplastics.

The net radiation heat flux to the plate is given by Siegel and Howell<sup>43</sup> as

$$q''_{rad} = \epsilon_o \epsilon_w F_{po} \sigma (T_o^4 - T_w^4) \quad (2.13)$$

where  $\sigma$  is the Stefan-Boltzmann constant and  $T_w$  is the local wall temperature.

Recalling Eq. (2.10), both conduction and radiation heat fluxes are now known, so the convection to the plate in the presence of the film can be found from

$$q''_{conv} = q''_{cond} - q''_{rad} \quad (2.14)$$

Figure 14 is a schematic of the energy balance on the plate describing the three heat transfer modes in the problem.

In general, convective heat transfer can be expressed as

$$q''_{conv} = h(T_{ref} - T_w) \quad (2.15)$$

where  $h$  is the convective heat transfer coefficient,  $T_{ref}$  is a reference temperature and  $T_w$  is the wall temperature.

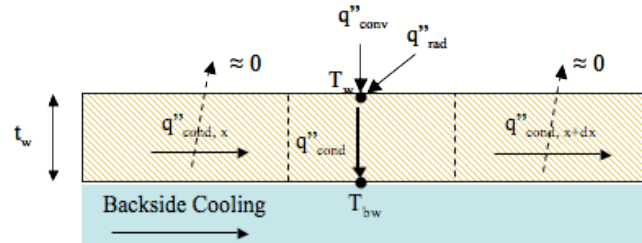


Figure 14. Schematic of heat transfer to plate

In film cooling, it is customary to let  $T_{ref}$  be the corresponding temperature such that  $q''_{conv} = 0$ , that is,  $T_{ref} = T_{aw}$ . Thus, Eq. (2.15) becomes

$$q''_{conv} = h(T_{aw,c} - T_w) \quad (2.16)$$

The left hand side has been obtained earlier from Eq. (2.14) while the temperatures on the right hand side have been obtained directly from experiments, where the adiabatic temperature has been corrected for deviations in the inlet conditions. Using this information, the convective heat transfer coefficient,  $h$ , can now be obtained,

$$h = \frac{q''_{conv}}{(T_{aw,c} - T_w)} \quad (2.17)$$

## 2.5 Uncertainty Analysis

Any experimental investigation involves a certain degree of uncertainty in the measurements. The accuracy and precision of the instrumentation play a key role as does error propagation due to derived quantities (i.e. heat transfer and convective heat transfer coefficients). In this section, the main sources of error for the quantitative data of the work are discussed. Where relevant, the classical statistical error propagation technique based on partial derivatives is presented.<sup>47</sup>

### 2.5.1 PIV

Because many parameters such as particle size, post processing algorithm, interrogation window sizes, etc. are involved in the calculations of velocity vectors, uncertainties in PIV are difficult to estimate. In general terms, following the guidelines presented by the manufacturer as well as those found in the literature, the accuracy of the system will be within 1-2%. These results are based on various validation schemes performed over several years, often involving “simulated” images and system calibration with carefully controlled flows. Detailed information on PIV uncertainty can be found in Raffel<sup>39</sup>. For the present work, all of the recommendations for particle physical size, particle image size, gate time, and post

processing scheme were followed. Careful calibration of the field of view was done prior to each run, in order to obtain accurate mappings of the 2-D space over which the images were taken, that is, properly mapping between pixel size and physical distance.

### 2.5.2 Gas Temperatures (microthermocouples)

Gas temperatures were measured with microthermocouples rated at  $\pm 0.25$  K. The non-dimensional temperature,  $\eta_{gas}$  given by

$$\eta_{gas} = \frac{T_\infty - T}{T_\infty - T_c} \quad (2.18)$$

is a derived quantity and is subject to error propagation. All of the temperatures on the right hand side of Eq. (2.18) are measured with the same thermocouple, and as such, all have the same accuracy. Recalling that for a quantity  $P$  depending on  $z$  measured quantities  $n_i$ , such that  $P = P(n_1, n_2, n_3, \dots, n_z)$ , then the uncertainty  $\sigma P$  is given by

$$\sigma P = \sqrt{\sum_{i=1}^z \left( \frac{\partial P}{\partial n_i} \sigma n_i \right)^2} \quad (2.19)$$

where  $\sigma n_i$  is the uncertainty associated with each measured quantity,  $n_i$ . Applying Eq. (2.19) to Eq. (2.18) and normalizing to express as percent error yields

$$\frac{\sigma \eta_{gas}}{\eta_{gas}} = \sqrt{\left( \frac{1}{T_c - T_\infty} \sigma T \right)^2 + \left( \frac{T - T_\infty}{(T_c - T_\infty)^2} \sigma T_c \right)^2 + \left( \frac{T - T_c}{(T_c - T_\infty)^2} \sigma T_\infty \right)^2} \quad (2.20)$$

In the limiting case where the thermocouple is in contact with the adiabatic wall,

$T = T_{aw}$ , and one recovers the expression for  $\eta_{aw}$ . Eq. (2.20) thus, also holds in the error propagation of the adiabatic wall effectiveness as well. For the present work, typical errors were on the order of  $< 3\%$  for  $\eta_{gas}$  and  $< 1\%$  for  $\eta_{aw}$ .

### 2.5.3 IR Thermography

In executing the in-situ IR calibration discussed in section (2.2.2), there are two main sources for error. First, the non-linear least squares fitting method will yield some residual resulting from the calibrated data being slightly deviated from the reference data. Evaluations of this residual in terms of percentage usually result in less than 1% error between the calibrated data point and its reference, which validates the use of the method. However, because thermocouple measurements are used as a reference, the calibrated data will reflect the error associated with the thermocouple plus the deviation resulting from the calibration method. If one can achieve a near-perfect calibration (IR data and reference data are within  $< 0.5\text{K}$  of each other), then IR calibrated data can be assumed to be within the thermocouple measurement error of  $\pm 0.25\text{ K}$ . This suggests that proper employment of the IR technique is the equivalent of having a thermocouple at each pixel of the IR image, with minimal loss of accuracy. Unfortunately, this optimum result is difficult to achieve and thus the calibration error dominates and one must be careful about the propagation of this error in derived quantities.

The IR measurements initially intended for this work presented some signal contamination, suggesting that other sources of error need to be addressed to obtain faithful results. Some potential causes have been identified, mostly associated with seeding particle deposits on the window. Once these issues are sorted out, the

calibration method from section (2.2.2) and the error analysis presented here, show that the IR technique has great potential to extend the spatial resolution of temperature measurements, with an associated decrease in accuracy that must be properly addressed, particularly in derived quantities.

#### 2.5.4 Heat Transfer

Another set of derived quantities that are subject to error propagation are the 3 modes of heat transfer as well as the convective heat transfer coefficient. First, the conductive heat transfer across the plate is a function of the plate's thermal conductivity, plate thickness, wall temperature,  $T_w$  and backside wall temperature,  $T_{bw}$ . Once again, applying Eq. (2.19) to Eq. (2.9) and rearranging as percent uncertainty, one obtains

$$\frac{\sigma q''_{cond}}{q''_{cond}} = \sqrt{\left(\frac{\sigma k_w}{k_w}\right)^2 + \left(\frac{\sigma t_w}{t_w}\right)^2 + \left(\frac{\sigma T_w}{T_{bw} - T_w}\right)^2 + \left(\frac{\sigma T_{bw}}{T_{bw} - T_w}\right)^2} \quad (2.21)$$

Given the values obtained in this work, typical error in the conductive heat transfer was on the order of 4% or less.

Next, the uncertainty associated with the radiation estimate is given by

$$\frac{\sigma q''_{rad}}{q''_{rad}} = \sqrt{\left(\frac{\sigma \epsilon_o}{\epsilon_o}\right)^2 + \left(\frac{\sigma \epsilon_w}{\epsilon_w}\right)^2 + \left(\frac{\sigma F_{wo}}{F_{wo}}\right)^2 + \left(\frac{4T_o^3}{T_o^4 - T_w^4} \sigma T_o\right)^2 + \left(\frac{4T_w^3}{T_o^4 - T_w^4} \sigma T_w\right)^2} \quad (2.22)$$

For this work, this relative uncertainty was on the order of 13% and was mostly sensitive to the uncertainty in the emissivity of the wall,  $\epsilon_w$ .

Finally, the error in the convective heat transfer is given by

$$\frac{\sigma q''_{conv}}{q''_{conv}} = \sqrt{\left(\frac{\sigma q''_{cond}}{q''_{cond}}\right)^2 \frac{q''_{cond}^2}{(q''_{cond} - q''_{rad})^2} + \left(\frac{\sigma q''_{rad}}{q''_{rad}}\right)^2 \frac{q''_{rad}^2}{(q''_{cond} - q''_{rad})^2}} \quad (2.23)$$

Because most of the contribution to  $q''_{conv}$  is due to  $q''_{cond}$ , the uncertainty in convective heat transfer is not greatly affected by that of the radiation estimate, and it was shown to be on the order of 5% for the values reported in this work.

Finally, the determination of the uncertainty in the heat transfer coefficient entails an intermediate step requiring the calculation of the absolute uncertainty in the corrected adiabatic wall temperature,  $T_{aw,c}$ , which is given by

$$\sigma T_{aw,c} = \sqrt{(\eta_{aw} \sigma T_{c,na})^2 + ((1 - \eta_{aw}) \sigma T_{\infty,na})^2 + ((T_{c,na} - T_{\infty,na}) \sigma \eta_{aw})^2} \quad (2.24)$$

Typically, this uncertainty was on the order of 0.6 K for the temperatures recorded in the experiments. Using this value, one can now obtain the uncertainty in the convective heat transfer coefficient,  $h$ , given by

$$\frac{\sigma h}{h} = \sqrt{\left( \frac{\sigma q''_{conv}}{q''_{conv}} \right)^2 + \left( \frac{\sigma T_{aw,c}}{T_{aw,c} - T_w} \right)^2 + \left( \frac{\sigma T_w}{T_{aw,c} - T_w} \right)^2} \quad (2.25)$$

The uncertainties in the convective heat transfer coefficient ranged from 60% in the near field to 8% in the far field. This is a result of Eq. 2.25 being highly sensitive to the temperature difference  $T_{aw,c} - T_w$ , which is on the order of 1K very close to the injection point. As this difference increases, the relative uncertainty decreases.

## Chapter 3: Results

This chapter focuses on the experimental results of this work. The first section presents basic flow characteristics from the  $m = 3.01$  case, which was of particular interest to modelers within the research group due to the ability of LES and RANS models to accurately capture wall-jet flow physics. Then, a more detailed analysis is presented to compare all cases.

### **3.1 Basic Flow Characteristics ( $m=3.01$ )**

In this section, flow visualization, PIV, thermal mixing and heat transfer characteristics will be discussed in an illustrative fashion of a typical high blowing ratio film cooling configuration.

#### **3.1.1 Flow Visualization**

The flow was visualized by seeding the coolant jet only and using the PIV system to illuminate and take several photographs of the flow. Two representative images corresponding to the near field  $0 < x/s < 25$  and the far field  $25 < x/s < 50$  are presented as Figure 15. In this case, one can see that the strong shear between the jet and the slower freestream rapidly develops turbulent structures. As these structures convect downstream, they grow in size and move away from the wall, clearly showing the jet's growth. In the farfield, large turbulent structures are evident and even some “shedding” of fluid is observed where small pockets of seeding detach from the main coolant flow and enter the mainstream. All of these observations are consistent with reported mechanisms for turbulent mixing and shear layer

development. It should be noted that one would expect to observe dilution of the seeding due to the mixing, but this is not evident in the images. It is very likely that dilution effects are masked by the non-uniform intensity distribution of the laser sheet. To observe dilution and mixing effects, a scalar concentration measurement method such as PLIF is the right choice.

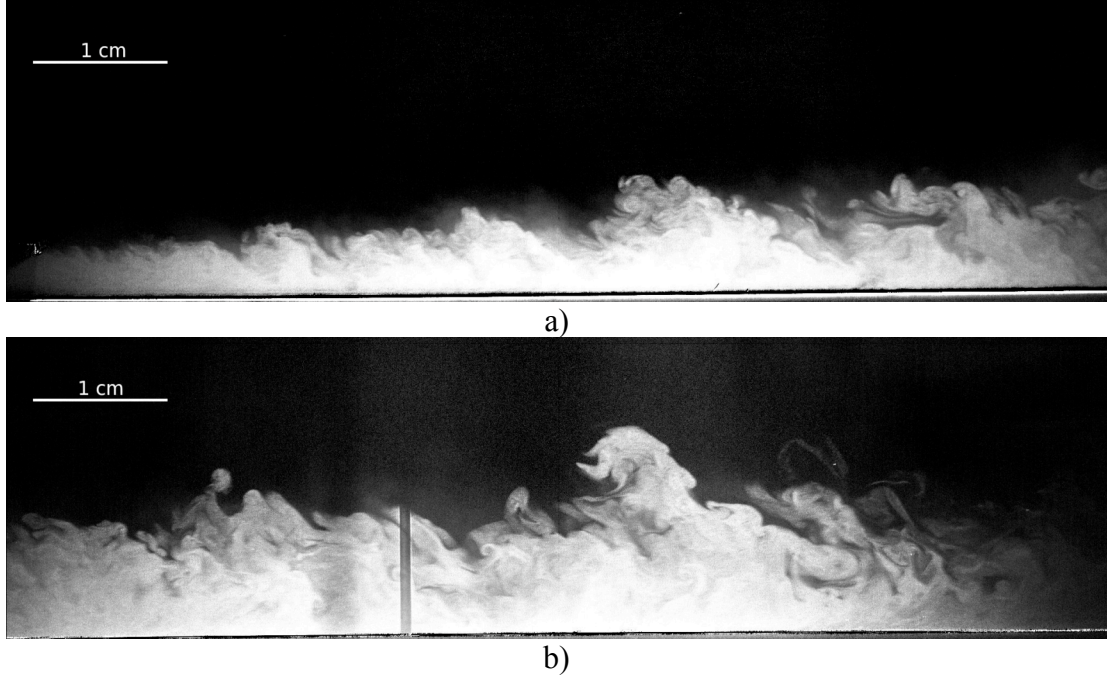


Figure 15. Flow visualization for  $m = 3.0$ . a) Nearfield,  $0 < x/s < 25$ , b) Farfield,  $0 < x/s < 50$

### 3.1.2 Kinematics

Figure 16 shows a characteristic mean velocity contour map obtained with the PIV technique in the near field,  $0 < x/s < 22.5$ . This contour map shows the strong x-component of the velocity vectors as well as the initial jet spread. Further post processing was used to obtain the velocity profiles shown in Figure 17. The first profile, corresponding to  $x/s = 1.2$  resembles a classical wall-jet. As one moves downstream, the jet's growth is observed as the peak velocity location shifts away

from the wall and the profile's shape continuously morphs. As expected, the peak velocity is also seen to decrease as one moves downstream. It should be noted that the slope of the profile far from the wall does not go to zero for locations  $x/s > 18.7$ . This is thought to be the result of flow entrainment through the test section window directly in front of the wall. This entrainment may cause acceleration of the mainstream flow and a reduction in the decay of the wall jet.

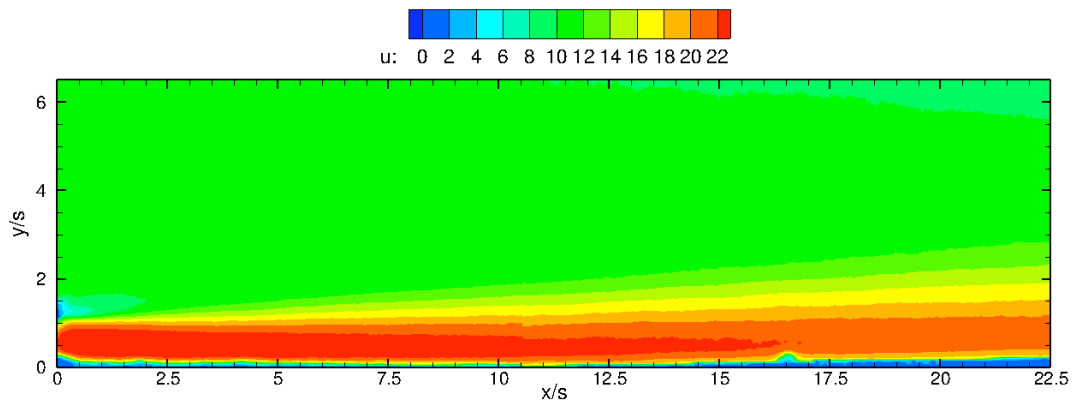


Figure 16. Near field contour map of velocity for  $m = 3.0$ .

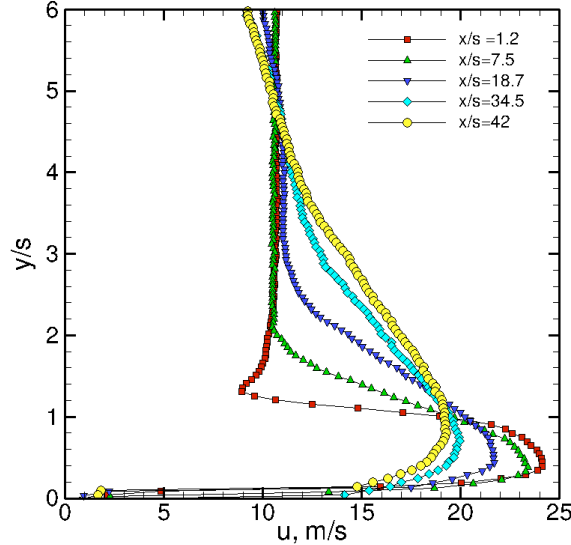


Figure 17. Profiles of x-component of velocity,  $u$ , for  $m = 3.0$ .

The RMS profiles of velocity components in Figure 18, show two regions of peak  $u_{rms}$ . The peak near the wall is consistent with wall induced turbulence, while the second peak is observed along the shear layer. As one moves downstream, the overall values of  $u_{rms}$  increase slightly, smoothing out this second peak, while the wall peak remains. This suggests that as the jet spreads, mixing enhances the growth of turbulent structures and smoothes out local peaks. Similar conclusions can be drawn from looking at profiles of  $v_{rms}$ . Far from the wall,  $u_{rms} \sim v_{rms}$ , suggesting the presence of isotropic turbulence. Given the 2-D characteristics of the PIV system, no measurements were made regarding the third component of RMS,  $w_{rms}$ , but due to the 3-D nature of turbulence, significant values of  $w_{rms}$  are expected and have been observed in film cooling simulations performed within the research group.

An interesting feature of PIV is the ability to obtain a velocity fluctuation field by subtracting the mean velocity field from any instantaneous velocity field. This enables one to uncover turbulent structures that are convected downstream at the

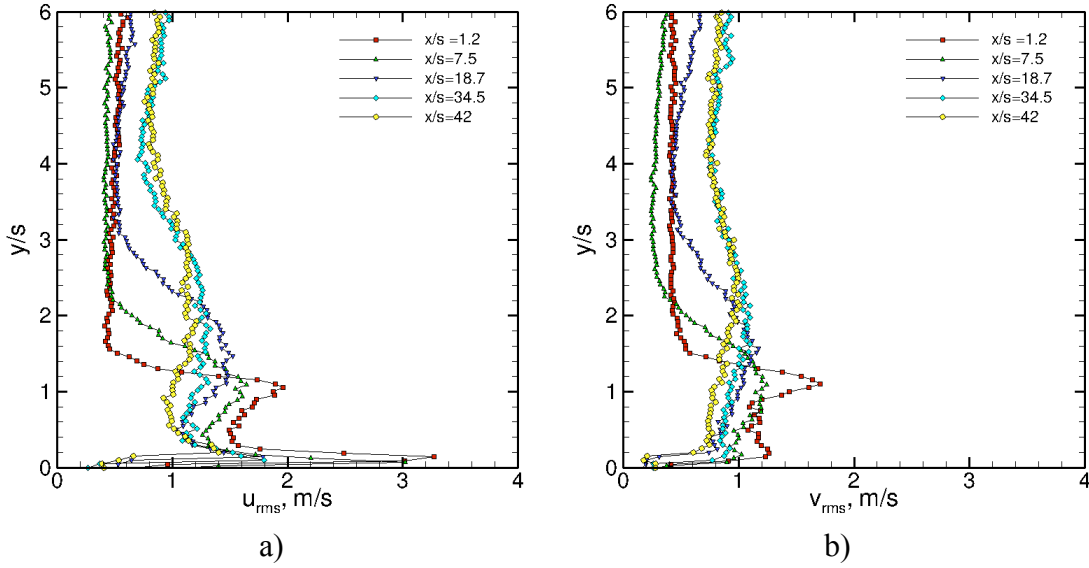


Figure 18. RMS profiles of 2-D components of velocity. a)  $u_{rms}$ , b)  $v_{rms}$

mean velocity, and are typically take the form of rollers. In general, the velocity fluctuation vector is given by

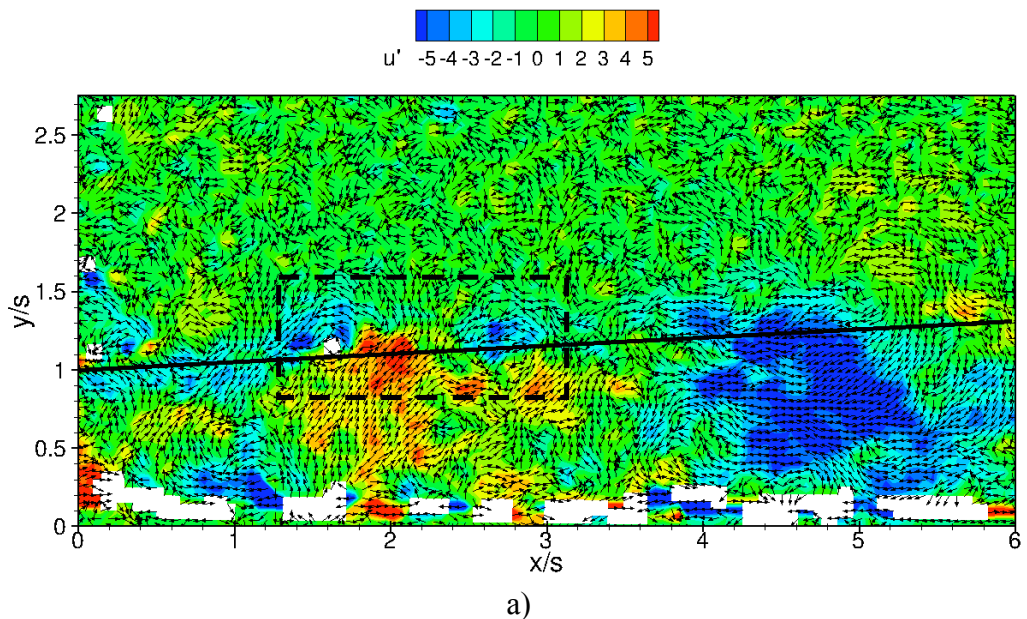
$$\vec{U}' = \vec{U} - \bar{\vec{U}} \quad (3.1)$$

where  $\vec{U}'$  is the fluctuation velocity vector,  $\bar{\vec{U}}$  is the mean velocity vector and  $\vec{U}$  is any instantaneous velocity vector.

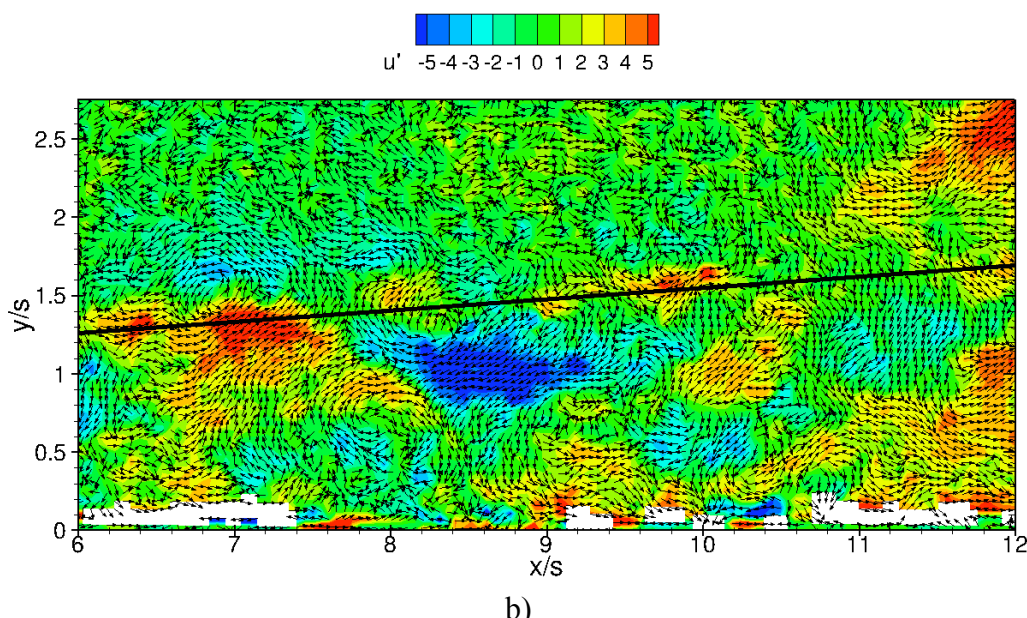
The flow visualization data discussed in section (3.1.1), suggests the roller structures have a counter-clockwise motion. A counter-clockwise roller will be marked by a cluster of negative  $u'$  vectors on top of a similar cluster of positive  $u'$  vectors.

Figure 19 (a) and (b) shows a typical velocity fluctuation field, while Figure 20 presents a close up of a single roller structure. White space corresponds to locations in the flowfield where not enough data was available to obtain an instantaneous fluctuation vector.

One would expect most of these rollers to appear along the interface between coolant and freestream, as this is the region of highest shear in the flowfield. In wall-jet theory<sup>17</sup>, the so called  $y_{1/2}$  location is defined as the y-coordinate where the velocity is exactly  $\frac{1}{2}$  of the difference between the jet's peak velocity and the freestream velocity. The location of  $y_{1/2}$  vs  $x/s$  is overlayed on top of Figure 19 and clearly shows that the rollers do indeed lie along this "jet spread" line. Also, as one moves downstream, some of these rollers tend to "pair up" with similar structures. Near wall structures are also identified. Finally, it should also be noted that the fact that this film cooling setup is not a true wall-jet (i.e. the freestream velocity does not vanish), the jet spread still behaves in a linear fashion.



a)



b)

Figure 19. Instantaneous velocity fluctuation vector fields, with  $u'$  contour visualization criterion and  $y_{1/2}$  location. a)  $0 < x/s < 6$ , b)  $0 < x/s < 12$

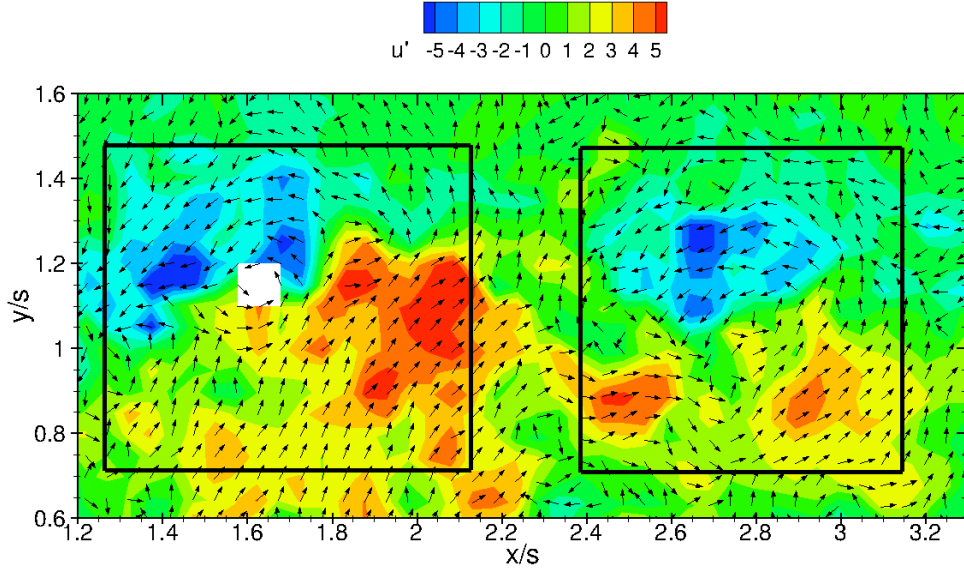


Figure 20. Closeup of roller structures highlighted in Figure 19.

### 3.1.3 Thermal mixing dynamics

It is clear that the kinematics of the flow correspond to the turbulent mixing of two co-flowing streams. One can expect, then, that the transport of properties will be directly related to the kinematics. Flow temperature is of particular interest, since it is ultimately the temperature difference between mainstream and coolant that governs film cooling performance. Figure 21 (a) shows the downstream evolution of the flow's thermal profiles for  $m = 3.01$ , under adiabatic conditions. A well characterized inlet is observed, with a sharp transition from coolant to mainstream conditions. As the flow visualization and kinematics suggested, fluid from the mainstream is entrained into the coolant stream, and coolant fluid is ejected. As a result of this fluid exchange, the temperatures at, and near the wall will rise, leading to a decrease in the difference between the extreme temperatures,  $\Delta T = T_\infty - T_{aw}$ . Simultaneously, the jet spreads, and a thermal gradient is established over a larger

wall normal distance,  $\Delta y$ . Both effects cause the thermal gradient  $\Delta T/\Delta y$  to get smaller and the result is observed as a steepening of the slopes of the thermal profiles.

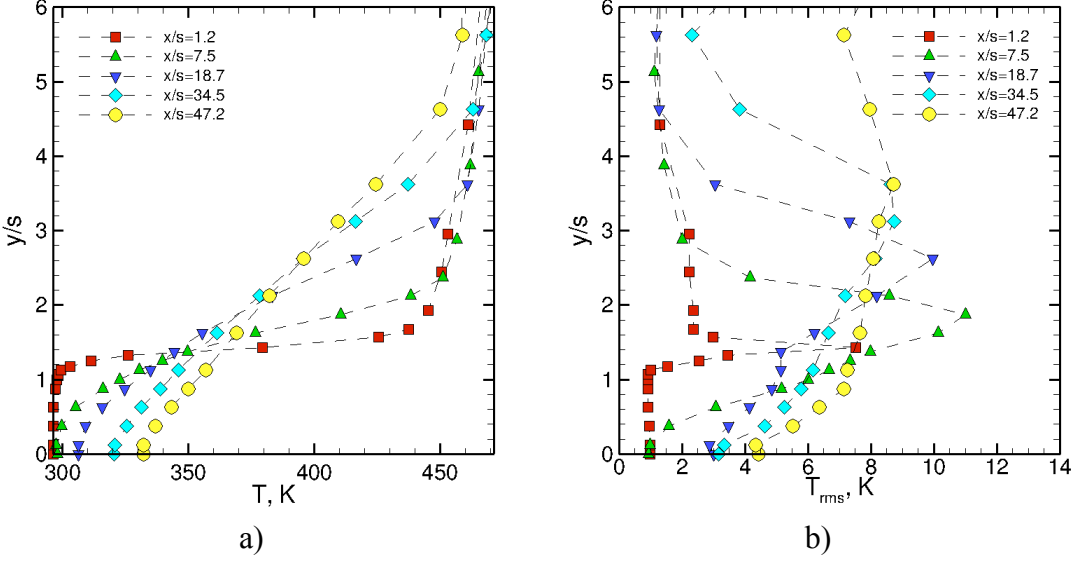


Figure 21. a) Raw temperature profiles for  $m = 3.0$  case, b) RMS of temperature

RMS values of temperature are shown in Figure 21 (b). As one moves downstream, temperature RMS values seem to increase, and the peak RMS location seems to shift away from the wall. This behavior can be explained by the growth of the turbulent structures, which allow for larger fluctuations, as well as the jet spread which tends to carry the largest turbulent structures away from the wall.

### 3.2 Case comparison

The experimental data spanning a large blowing ratio is well suited for a case comparison analysis where similarities and differences among cases can be studied. Because each case consists of an adiabatic and a non-adiabatic experiment, the analysis will be treated as 2 separate, but coupled problems. The adiabatic case will be viewed as a pure mixing scenario, where any relevant observations and findings will be an effect of mixing alone. The non-adiabatic case will be viewed as a change

of boundary condition on the previous case, where all observations will be an effect of this non-adiabatic boundary condition interacting with the flow.

### 3.2.1 Pure Mixing

Figure 22 shows the adiabatic wall effectiveness for all of the three studied blowing ratios. Near the injection region,  $x/s < 10$ , all of the cases behave similarly. However, further downstream, the  $m = 1.32$  case outperforms the others. This case corresponds to  $VR \sim 1.0$ , which should have the least shear at the interface. The  $m = 3.01$  case outperforms the  $m = 0.66$  case, indicating that a high blowing ratio performs better than a low blowing ratio.

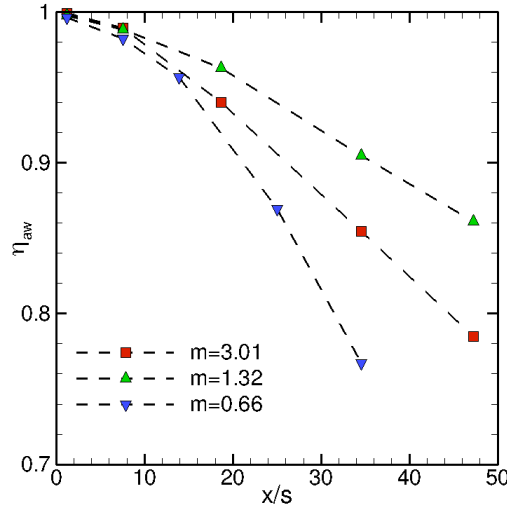


Figure 22. Adiabatic wall effectiveness,  $\eta_{aw}$  vs.  $x/s$ .

The underlying kinematics of all three flows seem to be the main cause of the observed behavior since the temperature ratios were nearly identical for all three cases. Therefore, it is important to analyze the flow visualization and kinematic data to gain a better understanding of the observed physics.

### 3.2.1.1 Flow Visualization

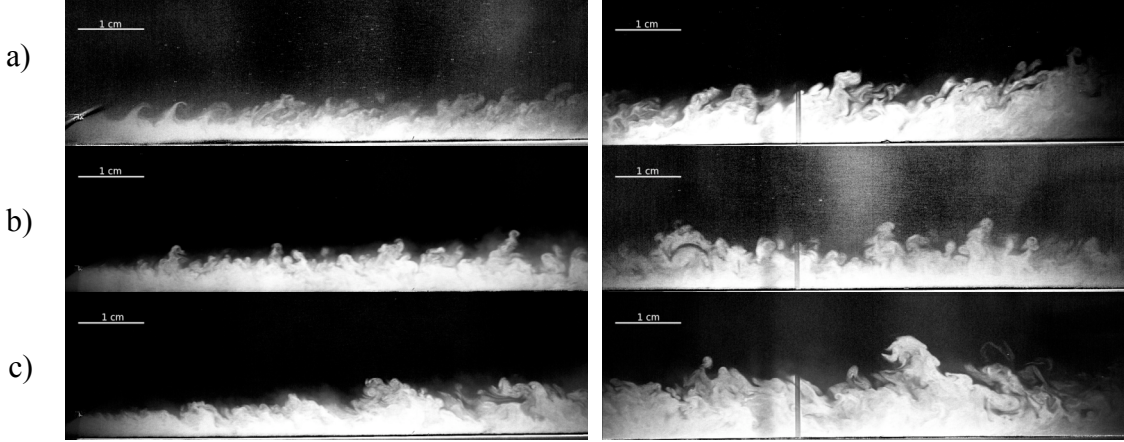


Figure 23. Flow visualization for all cases. a)  $m = 0.66$ , b)  $m = 1.32$ , c)  $m = 3.01$

Figure 23 shows the flow visualization data for all cases. In case a),  $m = 0.66$  and  $VR < 1.0$ , one observes how the fast mainstream flow drags along some of the slower moving coolant flow along. This shear motion at the interface results in clockwise roller structures that evolve into larger vortices, although the direction of motion is preserved. In case b),  $m = 1.31$  and  $VR \sim 1.0$ , one sees that no coherent roller structures are present, and that there does not seem to be a preferred direction for the flow at the interface to move along. Finally, for case c),  $m = 3.01$  and  $VR > 1.0$ , the fast moving coolant drags along the slower mainstream flow, causing the roller direction to be counterclockwise. Again, these structures grow downstream, but preserve their original direction. A closer look at these structures is shown in Figure 24.

The roller structure in Figure 24 (a) is taken from the  $VR < 1.0$  case. Here, low speed flow from the coolant is accelerated forward and away from the wall. As a reaction, some high speed flow from the mainstream is decelerated towards the wall. The

directions of this motion exchange are highlighted in the Figure and this motion is what sets up the clockwise direction of the roller. Figure 24 (b) does not show any particular direction, so one can only infer that fluid exchange between coolant and mainstream is occurring without a preferred direction. In Figure 24 (c), the initial case is reversed. Low speed flow from the mainstream is accelerated forward and towards the wall, while high speed coolant flow is decelerated and moved away from the wall. This establishes the counterclockwise motion discussed earlier in section 3.1. From these results, it appears that for  $VR \sim 1.0$ , the lack of a preferred direction is a direct effect of minimum shear at the interface, and thus, there is a lack of strong turbulent structures. Because these “rollers” are ultimately responsible for inducing the mixing as they grow and convect downstream, it seems natural that the flow

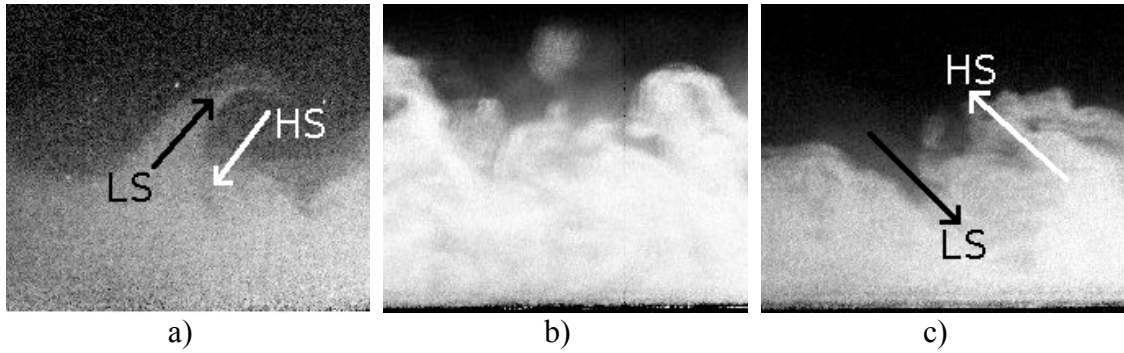


Figure 24. Turbulent structures due to shear. a) Clockwise roller for  $VR < 1.0$ , b) no preference for  $VR \sim 1.0$ , c) counterclockwise roller for  $VR > 1.0$ .

in case (b) would not mix as fast as either of the two remaining cases. This reduced rate of entrainment of hot fluid towards the wall results in a higher adiabatic wall effectiveness.

### 3.1.1.2 Kinematics

The distinct kinematic characteristics of each of the flows provides further understanding of the role of mixing on film cooling performance. Figure 25 shows the inlet velocity profiles for each of the cases.

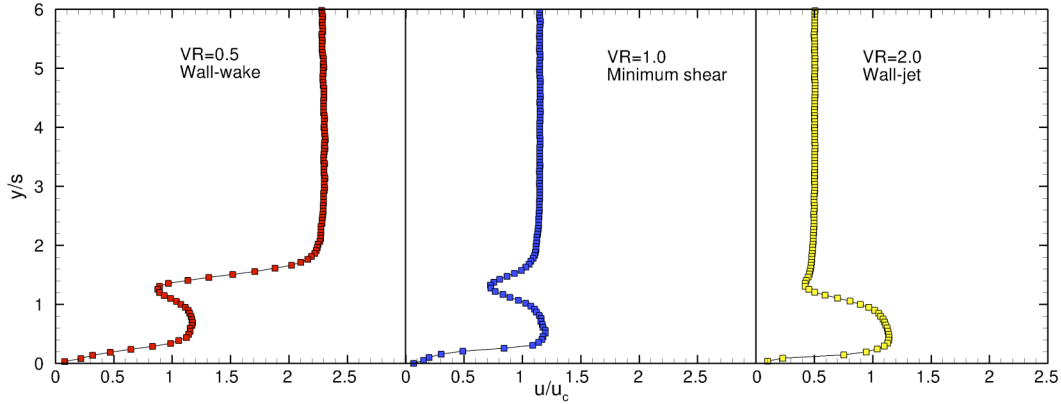


Figure 25. Inlet velocity profiles for all cases.

For the so called wall-wake flow,  $VR < 1.0$ , the coolant stream lags with respect to the freestream, and a slight wake is observed due to louver effects. The large difference in velocities suggests strong shear at the interface. For the minimum shear flow,  $VR \sim 1.0$ , and, as the name implies, minimum shear is expected along the interface. For the wall-jet case,  $VR > 1.0$ , the situation from the first case is reversed, and one expects strong shear at the interface. One would expect these profiles to deform as mixing occurs.

Figure 26 shows the velocity profiles for the same cases far downstream of the injection, at  $x/s \sim 47.2$ . The effect of the film is still felt in all cases, and the profiles have not yet achieved any degree of boundary layer similarity. In the wall-wake, most of the high speed flow remains in the mainstream. The opposite is true in the wall-jet case. The minimum shear case closely resembles a turbulent boundary layer profile.

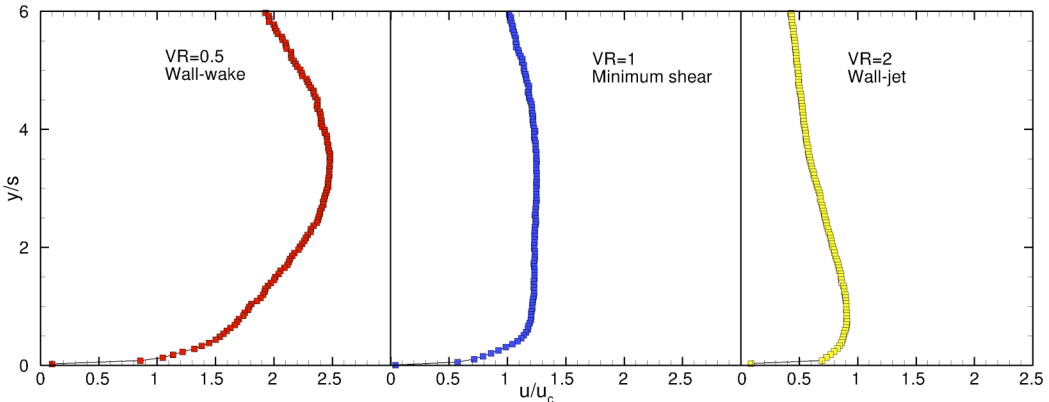


Figure 26. Velocity profiles far downstream,  $x/s \sim 47.2$ , for all cases.

The strongest shape transformations occurred in the wall-wake and wall-jet cases. Both of these transformations required strong momentum exchange to achieve the respective shapes portrayed in Figure 26, while the minimum shear case required the least effort. Once again, this suggests high mixing levels in the extreme cases, since strong mixing is required to support the observed momentum exchange. By similar reasoning, the minimum shear case required less momentum exchange for the deformation, and thus lower mixing levels are expected.

Far away from the wall, the profiles exhibit some unexpected behavior where the velocities do not approach a perfectly vertical distribution. Careful inspection of the data and test section suggest that this is an effect of flow entrainment through the IR transparent window. While the effects of this secondary flow do not seem to significantly alter near-wall measurements, they do pose some problems for model validation. For a complete summary of kinematic data for all cases, the reader is referred to Appendix A.

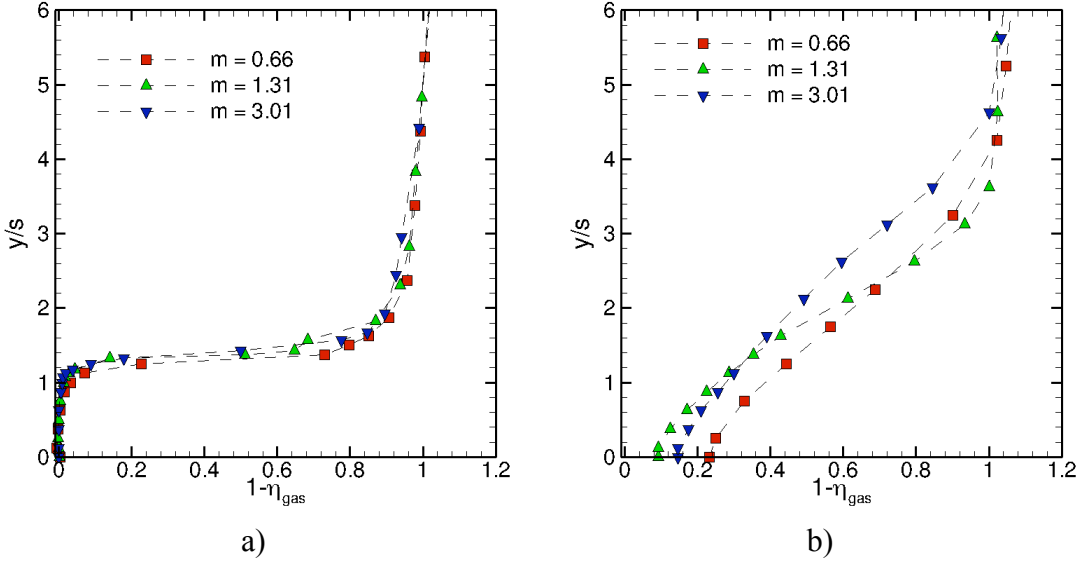


Figure 27. a) Inlet thermal profiles comparison, b) thermal profiles at  $x/s = 34.5$

### 3.1.1.3 Thermal Mixing

Temperature profiles were obtained at 5 distinct downstream locations in each case. Figure 27 (a) shows the similarity of the inlet profiles for the 3 cases. Due to this initial similarity, one would expect that any differences in the profiles far downstream arise from the turbulent mixing and kinematics of each particular case. Figure 27 (b) shows the thermal profiles at  $x/s = 47.2$ . In both figures, the near-wall gradients show that an adiabatic condition is well established for all cases.

Figure 27 (b) provides some great insight into the behavior of each particular flow. The minimum shear type flow,  $\text{VR} \sim 1.0$ ,  $m = 1.31$ , presents the strongest thermal gradient,  $dT/dy$ , in the mixing layer region. This suggests little mixing compared to the other cases. The wall-wake case,  $\text{VR} < 1.0$ ,  $m = 0.66$ , shows lower values of  $\eta_{\text{gas}}$  than the minimum shear case for  $y/s < 2.4$ . This suggests that the flow near the wall is relatively hotter in the wall-wake case as a result of stronger mixing. The wall-jet

case,  $VR > 1.0$ ,  $m = 3.01$  also shows this trend of relatively hotter near wall flow. However, this effect is confined to a smaller near-wall region compared to the wall-wake (about  $y/s < 1.2$ ). For  $y/s > 1.2$ , the wall-jet case actually shows relatively cooler flow. This is expected because the coolant flow in the wall jet case spreads away from the wall and mixes strongly with the mainstream, effectively reducing the mainstream flow's temperature. The distinct kinematics of each case ultimately determine the transport of enthalpy in the flow, via the transport of hot fluid towards the wall. What Figure 27 (a) and (b) shows is that for initially similar thermal profiles, flows with velocity profiles of either a wall-wake or a wall-jet type result in hotter near-wall fluid with respect to a minimum shear type flow. This suggests that the initial shear from either a wall-jet or a wall-wake flow develops higher mixing levels that draw hot fluid toward the wall. The minimum shear flow delays this initial mixing. As a result, it is able to keep cooler flow near the wall and achieve a higher effectiveness. RMS profiles of temperature confirm this hypothesis. The minimum shear case has the lowest values of near-wall RMS compared to either of the other two cases. This shows that the mixing delay due to minimum shear results in less strong near wall mixing, and a better film cooling performance. For a complete summary of thermal mixing data, the reader is referred to Appendix B.

### **3.1.2 Non-adiabatic boundary condition**

In this section, the effects of the non-adiabatic boundary condition are examined. The data in Appendix B, shows small but detectable changes in the mean temperature profiles. Their shape and behavior with downstream distance is virtually identical to the adiabatic case except for the lower wall temperature resulting from the backside

cooling. Since it was shown earlier that thermal transport and kinematics were coupled, this similarity in the thermal behaviors of the flow reinforces the concept that the boundary condition has no appreciable effect on the kinematics.

The most important feature of the non-adiabatic condition is that it provides wall temperature data that can be used to obtain heat transfer information that cannot be measured from adiabatic experiments alone. This heat transfer data is not only valuable for further insight, but also for modeling efforts.

Recalling Eqs. 2.9 and 2.16, it was shown that the adiabatic wall temperature,  $T_{aw}$ , the non-adiabatic wall temperature,  $T_w$ , and the backside wall temperature,  $T_{bw}$  determine the heat transfer of the film cooling problem. Figure 28 shows the downstream evolution of these temperatures for each case. Coolant temperatures are provided as reference. In the absence of film cooling, one would expect the wall temperature to be on the order of the mainstream temperature ( $> 430\text{K}$  for all cases). Figure 28 shows that film cooling substantially reduces the wall temperature, as  $T_{aw}$  is significantly less than the reference mainstream temperature,  $T_\infty$ . Backside cooling enhances this protection, further lowering the wall temperature such that  $T_w < T_{aw}$ .

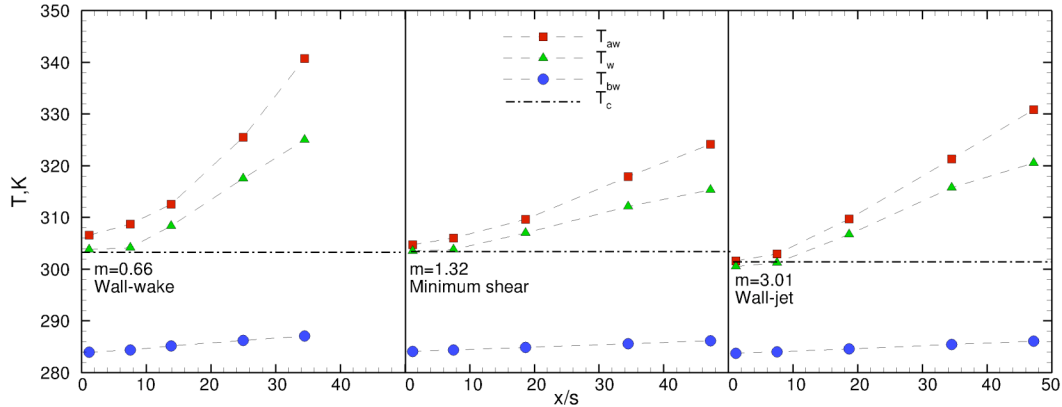


Figure 28. Governing temperatures for heat transfer problem.

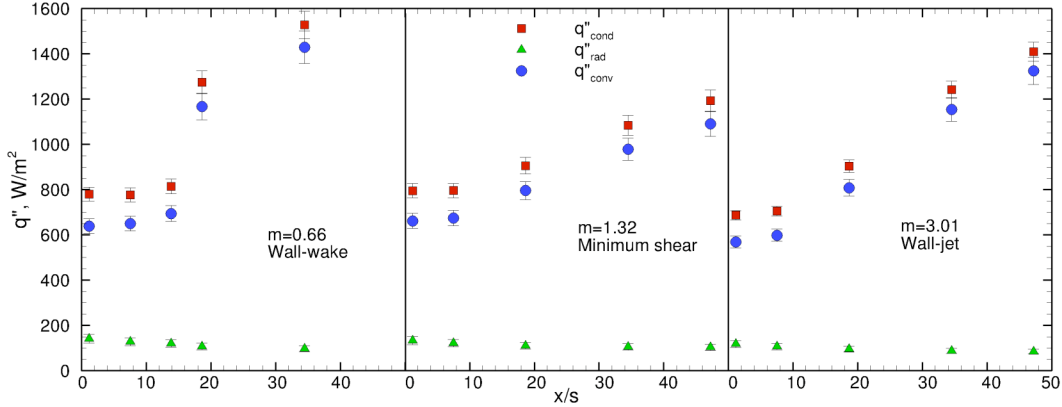


Figure 29. Conjugate heat transfer

Figure 29 shows the conjugate heat transfer for all cases. Radiation heat transfer shows relatively low values. The minimum shear case,  $\text{VR} \sim 1.0$  exhibits the lowest heat transfer to the wall, followed by the wall-jet,  $\text{VR} > 1.0$  and wall-wake,  $\text{VR} < 1.0$  cases respectively. This is consistent with the adiabatic wall temperature measurements. It is worth noting that the heat transfer and adiabatic wall temperature measurements were obtained independently yet show similar trends. This correlation between adiabatic and non-adiabatic cases further confirms the idea that the minimum shear type of flow provides optimum film cooling performance, not only from an adiabatic wall effectiveness perspective, but also from a heat flux perspective. This similar behavior provides confidence in coupling the convective heat flux data with adiabatic wall temperature measurements to obtain the distribution of the convective heat transfer coefficient,  $h$ . The results are presented in Figure 30.

For  $\text{VR} \sim 1.0$  and  $\text{VR} > 1.0$ , the behaviors of  $h$  vs  $x/s$  are quite similar in both trend and magnitude. For  $\text{VR} < 1.0$ , the values of  $h$  are generally smaller, and a trend discontinuity is observed in the vicinity of  $x/s = 10$ . However, the low blowing ratio case was also the case with highest heat transfer. It is worth noticing that the low

blowing ratio case had a much lower coolant injection velocity, whereas the other two cases had similar coolant injection velocities. Based on these observations, the fact that the case with the highest heat transfer showed the lowest value of  $h$  suggests that the overall value of  $h$  is governed by the coolant injection velocity alone, while the resulting heat transfer is governed by the velocity ratio and corresponding wall temperatures. In fact, Lefebvre suggested a correlation for  $h$  that depends strongly on the coolant injection velocity.

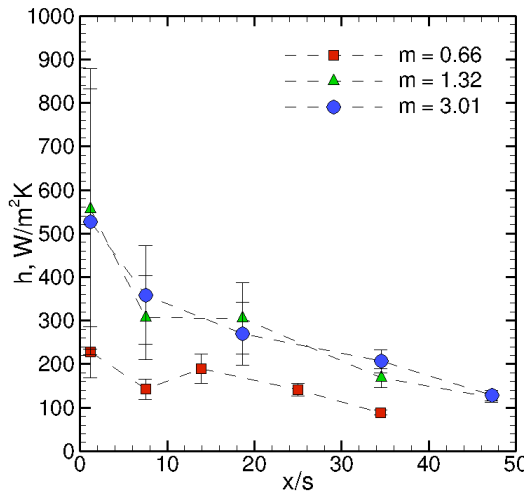


Figure 30. Convective heat transfer coefficient,  $h$ .

It is also worth pointing out that at the injection location, both  $T_{aw}$  and  $T_w$  have similar values, and thus a large error is obtained. Further downstream, this error decreases as the temperature difference increases. This large error raises a question about the usefulness of  $h$ , particularly since modern CFD codes can accurately predict heat transfer directly, and experimental heat transfer can be obtained with much less error. A non-dimensional version of the heat transfer coefficient can be defined in terms of mainstream conditions as

$$St_{\infty} = \frac{h}{\rho_{\infty} C_{p,\infty} U_{\infty}} \quad (3.1)$$

where  $St$  is the Stanton number. The Reynolds number based on downstream location and mainstream conditions is given by

$$Re_x = \frac{U_{\infty} x}{v_{\infty}} \quad (3.2)$$

Figure 31 is a plot of  $St_{\infty}$  vs.  $Re_x$ . It shows that initially, the Stanton number is a strong function of the velocity ratio, but far downstream all curves approach a similar value. The usefulness of this non-dimensionalization lies in the fact that it uses well-established mainstream conditions, instead of the local near-wall conditions that actually govern the heat flux but are in practice more difficult to quantify. In this way, recovering the convective heat

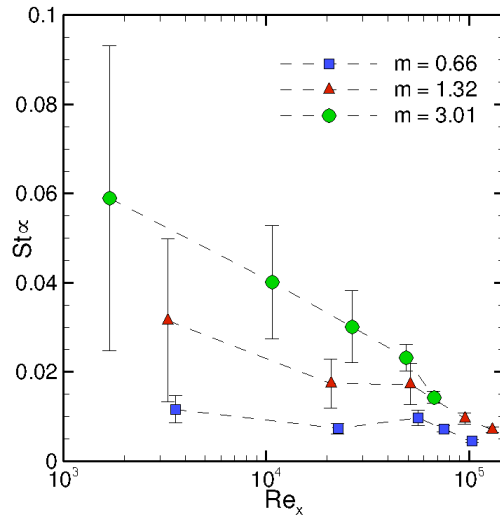


Figure 31.  $St_{\infty}$  vs.  $Re_x$

transfer coefficient for a given blowing ratio becomes much simpler, as one is only required to know about mainstream conditions.

## Chapter 4: Conclusions

This work is one of the first comprehensive (kinematics + thermal mixing + wall temperatures + heat transfer) slot film cooling studies over a wide blowing ratio range to be reported in the literature. The comprehensive and correlated nature of the data has allowed for an in-depth study of the coupling of kinematics and thermal transport in slot film cooling flows. The experimental study has made extensive use of minimally intrusive diagnostic techniques in order to characterize slot film cooling flows. The data obtained has been analyzed to gain further insight into film cooling physics, and has also served as reference for an in-house model development and validation within our research group. Comprehensive measurements including flow visualization, Particle Image Velocimetry, wall surface and flow temperature measurements were obtained, and challenges associated with each technique were addressed.

### **4.1 Summary of results**

The main results from the analysis of the experimental data are summarized below.

#### **4.1.1 Adiabatic wall effectiveness**

- The adiabatic wall effectiveness decreases with downstream distance. Among all cases, the VR  $\sim 1.0$  case performed significantly better than the remaining cases.
- The high blowing ratio case, VR  $> 1.0$ , outperformed the low blowing ratio case, VR  $< 1.0$ .

#### **4.1.1 Flow visualization**

- The turbulent structures arising from viscous shear at the mainstream and coolant interface were visualized by using a planar laser sheet and a seeded coolant flow.
- The wall-wake case,  $VR < 1.0$  exhibited clockwise roller structures, associated with the faster moving mainstream.
- The wall-jet case,  $VR > 1.0$ , exhibited counterclockwise roller structures, associated with the faster moving coolant stream.
- The minimum shear case,  $VR \sim 1.0$ , did not exhibit any well defined roller structures.

#### **4.1.2 Kinematics**

- Particle image velocimetry was used to obtain flow velocities with a spatial resolution of  $< 1.0$  mm.
- Statistical analysis performed on the wall-jet,  $VR > 1.0$ , case confirmed the direction of the roller structures visualized previously. A wall-jet analysis showed that these rollers grow and spread along the  $y_{1/2}$  line, characteristic of wall jet spread.
- Analysis of the evolution of velocity profiles with downstream location for each case show that the extreme cases require high levels of momentum exchange associated with high levels of turbulent mixing. In contrast, the minimum shear case did not exhibit significant deformation of the velocity profile, suggesting less turbulent mixing occurs.

#### 4.1.3 Thermal mixing

- Inlet thermal profiles were similar for all cases. Far downstream, however, the minimum shear case presents a region of cooler flow near the wall, compared to the other two cases.
- Near wall temperature RMS values were lowest for the minimum shear case, suggesting lower turbulent mixing strength for this case.
- The presence of a non adiabatic boundary condition results in lower wall and flow temperatures, but general trends are preserved from adiabatic cases.

#### 4.1.4 Heat Transfer

- Heat transfer trends obtained independently from adiabatic measurements, agree with adiabatic wall effectiveness measurements. The minimum shear case,  $VR \sim 1.0$ , presents the lowest heat flux, followed by the  $VR > 1.0$ , and  $VR < 1.0$  respectively.
- The convective heat transfer coefficient,  $h$ , was obtained for all cases, albeit with significant measurement error. The evolution of  $h$  vs.  $x/s$  seems to be a function of coolant injection velocity alone. Furthermore, the error associated with the calculation of  $h$  and the availability of CFD codes raises questions about its usefulness.
- The Stanton number based on mainstream conditions was also obtained. The evolution of  $St$  vs.  $Re_x$ , where  $Re_x$  is based on mainstream conditions as well, suggests that near the injection, the  $St$  behavior is a strong function of the

velocity ratio. Far downstream, this effect vanishes and  $St$  approaches a similar value for all cases

The aforementioned observations suggest that film cooling performance is strongly affected by the shear at the interface between coolant and mainstream flows. For flows with minimum shear, turbulent mixing structures are not well established and mixing is delayed, providing the best overall performance in terms of adiabatic effectiveness and heat transfer. For high shear flows, these structures have a well defined shape and their growth is readily observed. However, having an initial high momentum in the coolant ( $VR > 1.0$ ) results in improved performance with respect to the opposite case.

The large errors associated with the measurement of the convective heat transfer coefficient,  $h$ , along with the lack of accurate correlations in the literature, and the ability of modern CFD codes to accurately calculate heat transfer, suggests that the validity of  $h$  as a parameter for film cooling is questionable at best. Instead, direct experimental heat transfer measurements provide a more valuable tool for model development and validation.

#### **4.2 Suggestions for future research**

The current work suggests that there is room for improvement and further research on several fronts. In terms of diagnostics, improving the accuracy of an IR thermography system such that an uncontaminated signal is obtained, and the fitting procedure results in minimal residuals (IR data and reference data  $< 1K$  of each other) is equivalent to extending the spatial resolution of the wall surface and heat transfer measurements, obtaining a complete 2-D distribution of said quantities. Fixing the

problem of flow entrainment through the thermally transparent window will minimize model validation issues due to discrepancies between experimental and numerical results.

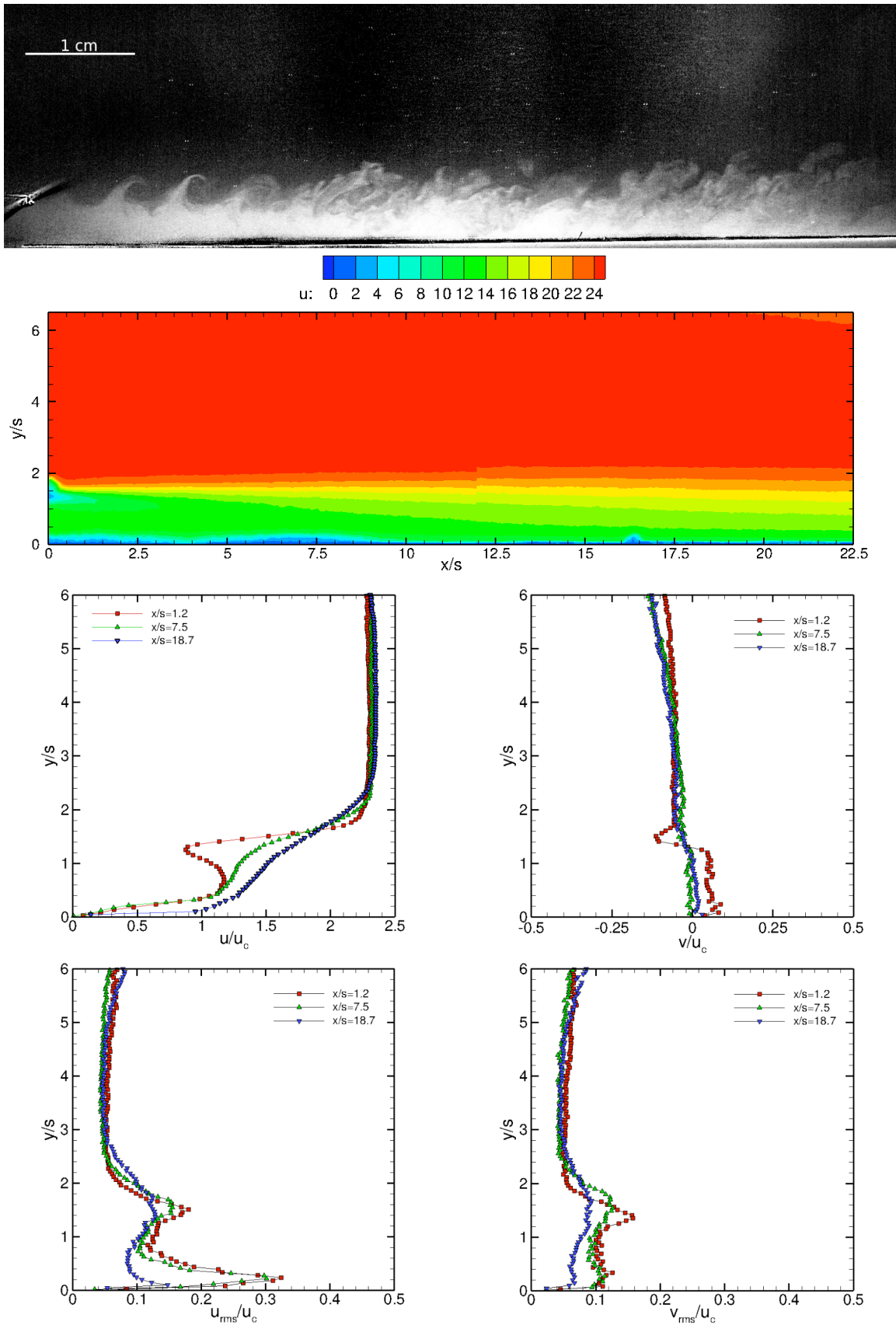
Investigating the effects of louver thickness, injection angle, slot height and inlet turbulence intensities can also be performed with minimal modifications to the test section.

The lessons learned about implementing minimally intrusive diagnostics in film cooling flows can also be extended to supersonic film cooling. Although a new facility is needed, a similar comprehensive approach where kinematics, wall temperatures and heat transfer are measured will be very useful for understanding film cooling performance in supersonic applications like rocket thrust chambers + nozzle extensions.

## Appendix A. Kinematics

This appendix summarizes all of the kinematic data obtained for the present study. A diagram of the layout is presented here to aid the reader in the understanding of the data.

	a) Flow visualization image
	b) Mean contour of x-component of velocity, $u$
c) Normalized x-component of velocity, $u/u_c$	d) Normalized y-component of velocity, $v/u_c$
e) Normalized x-component of RMS, $u_{rms}/u_c$	f) Normalized y-component of RMS, $v_{rms}/u_c$



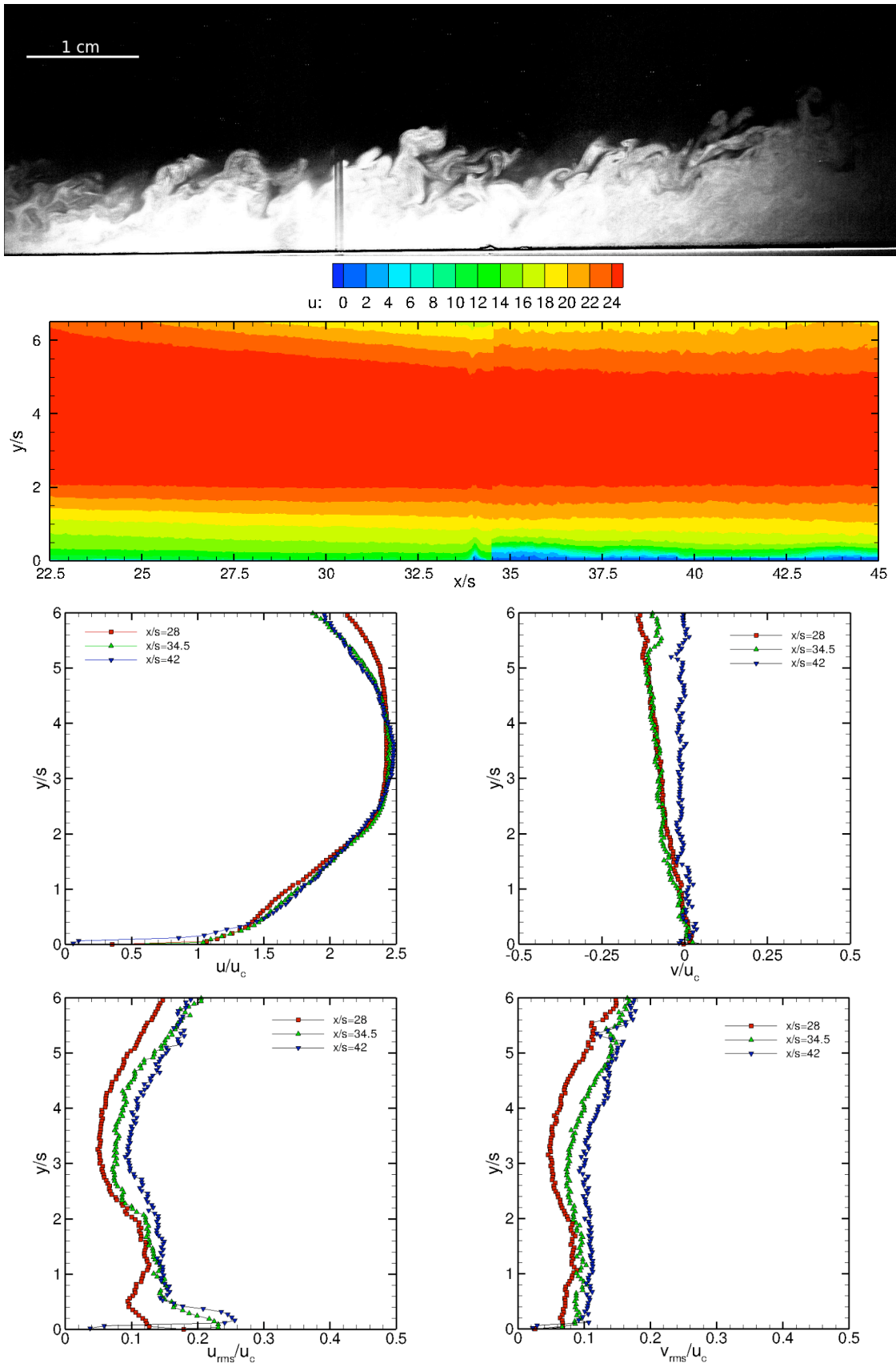
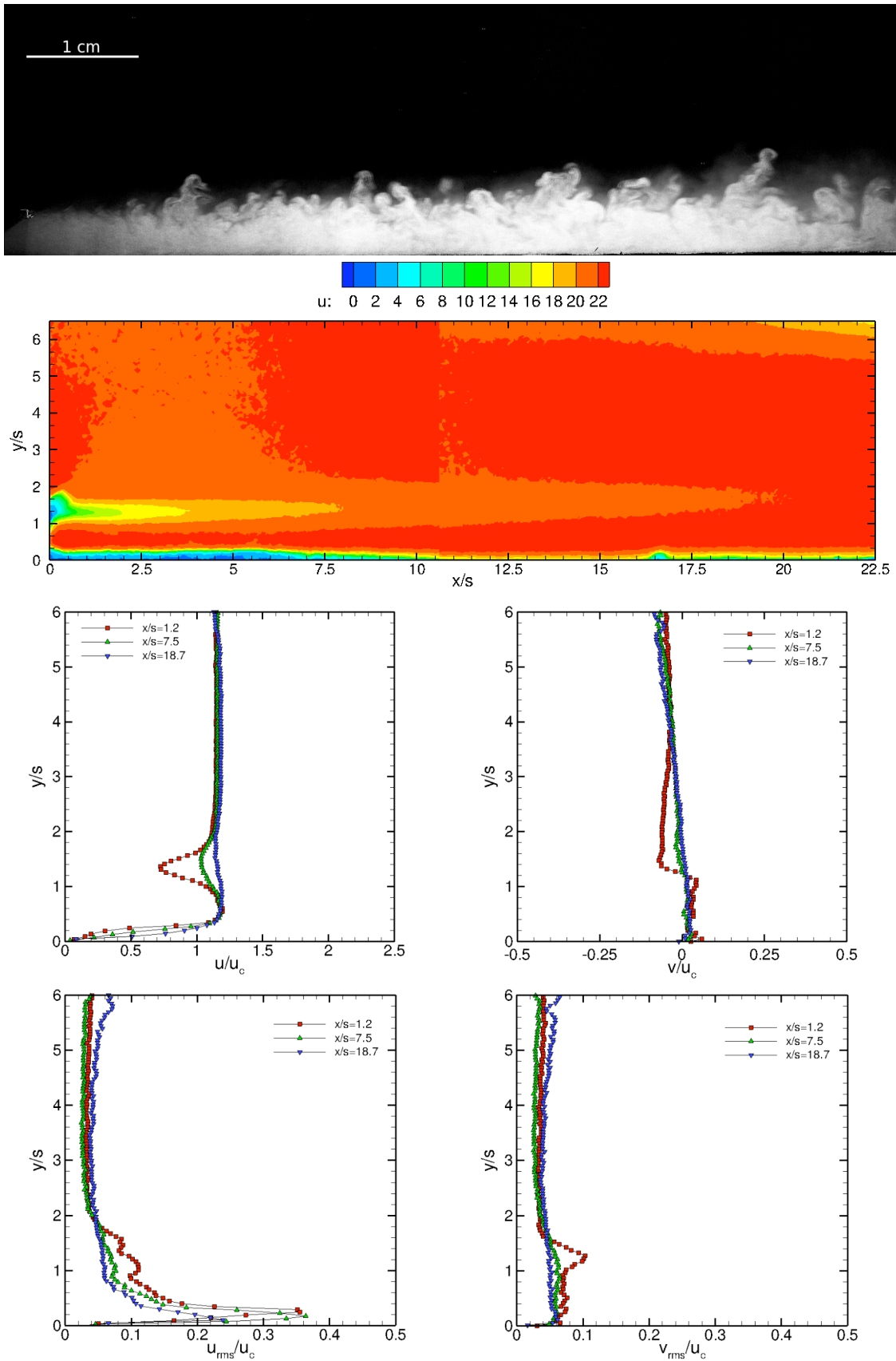


Figure A. 2. a) - f) VR = 0.5 Far Field



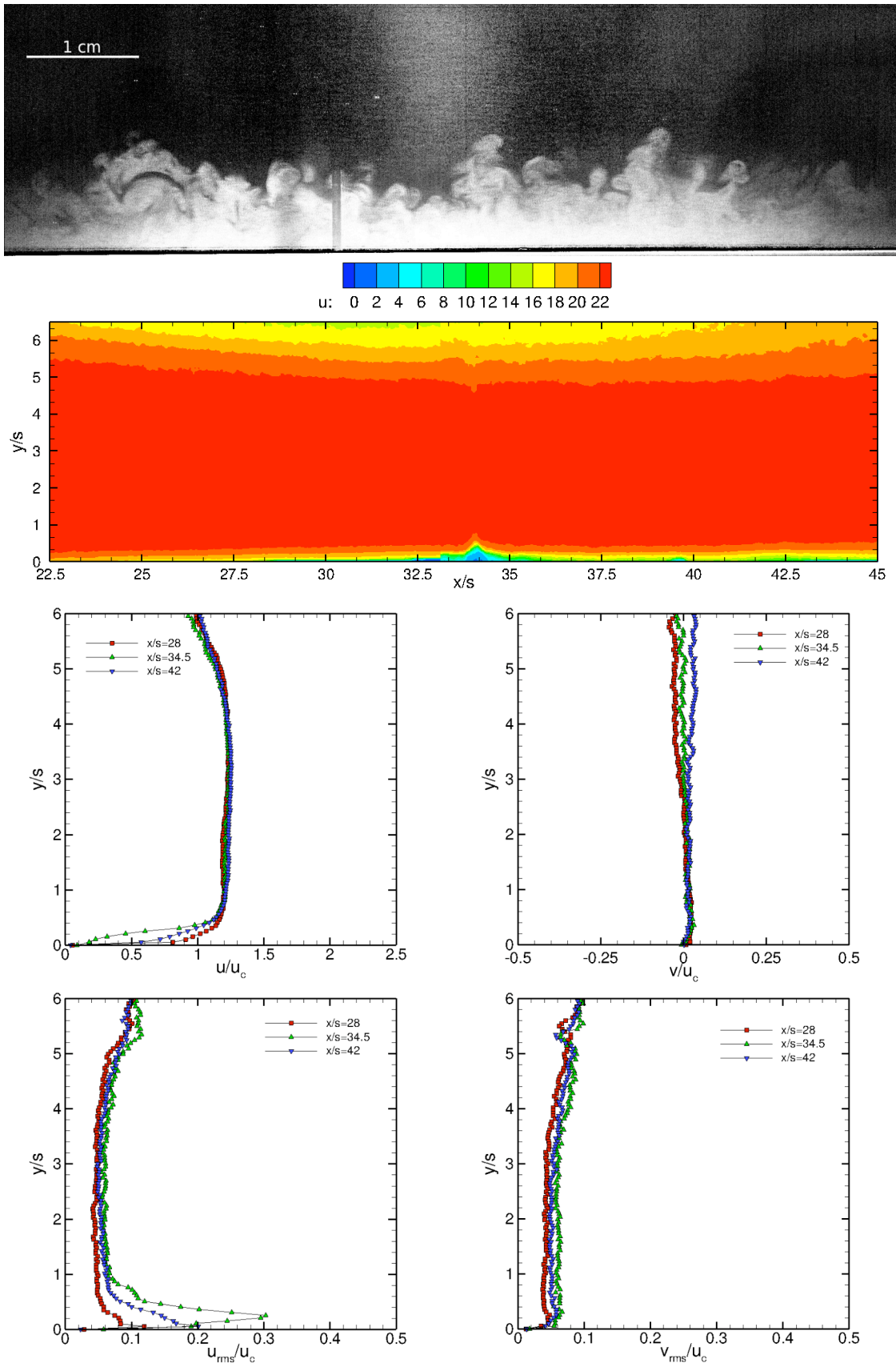
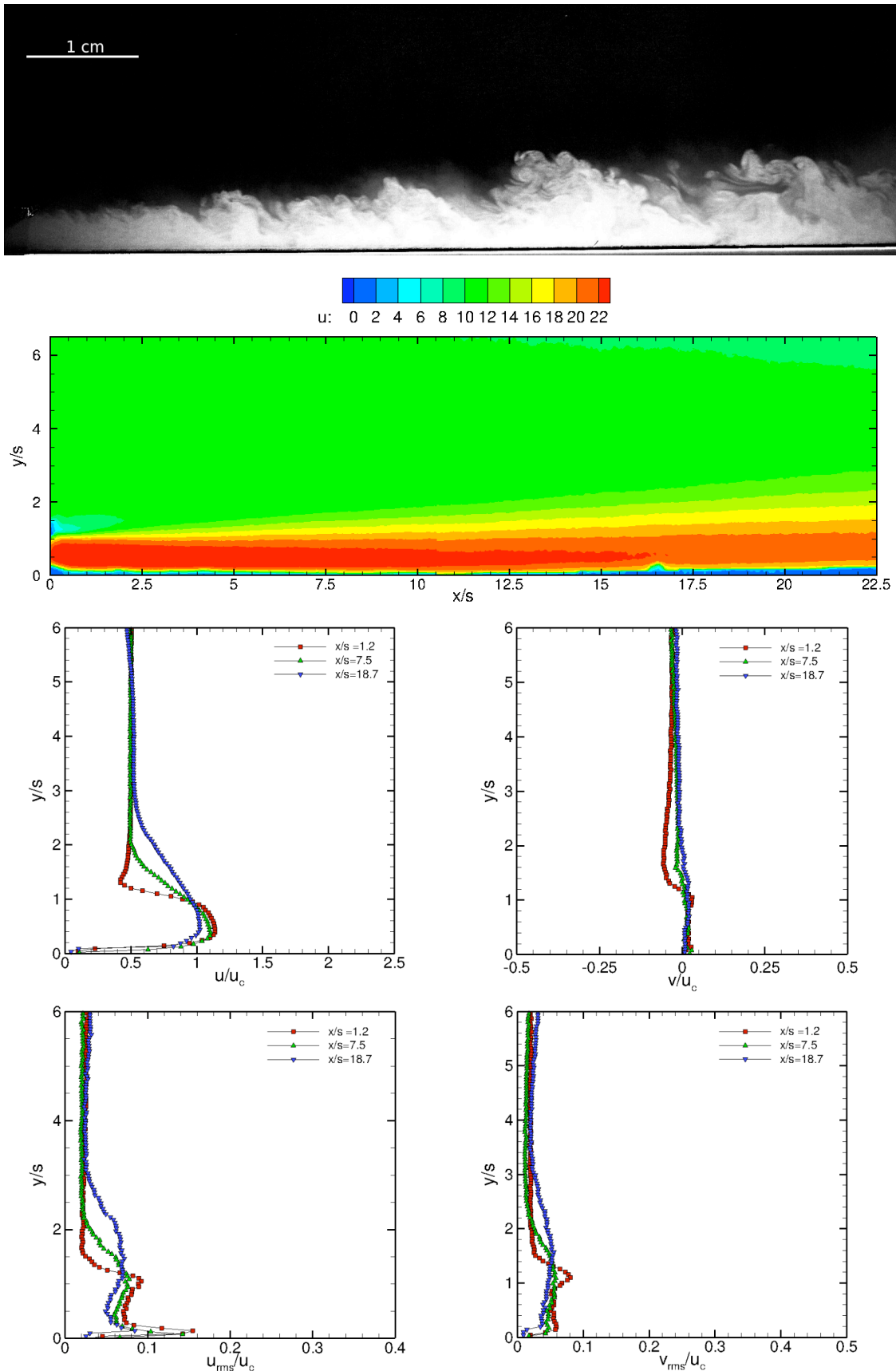


Figure A. 4. a) - f) VR = 1.0 Far Field



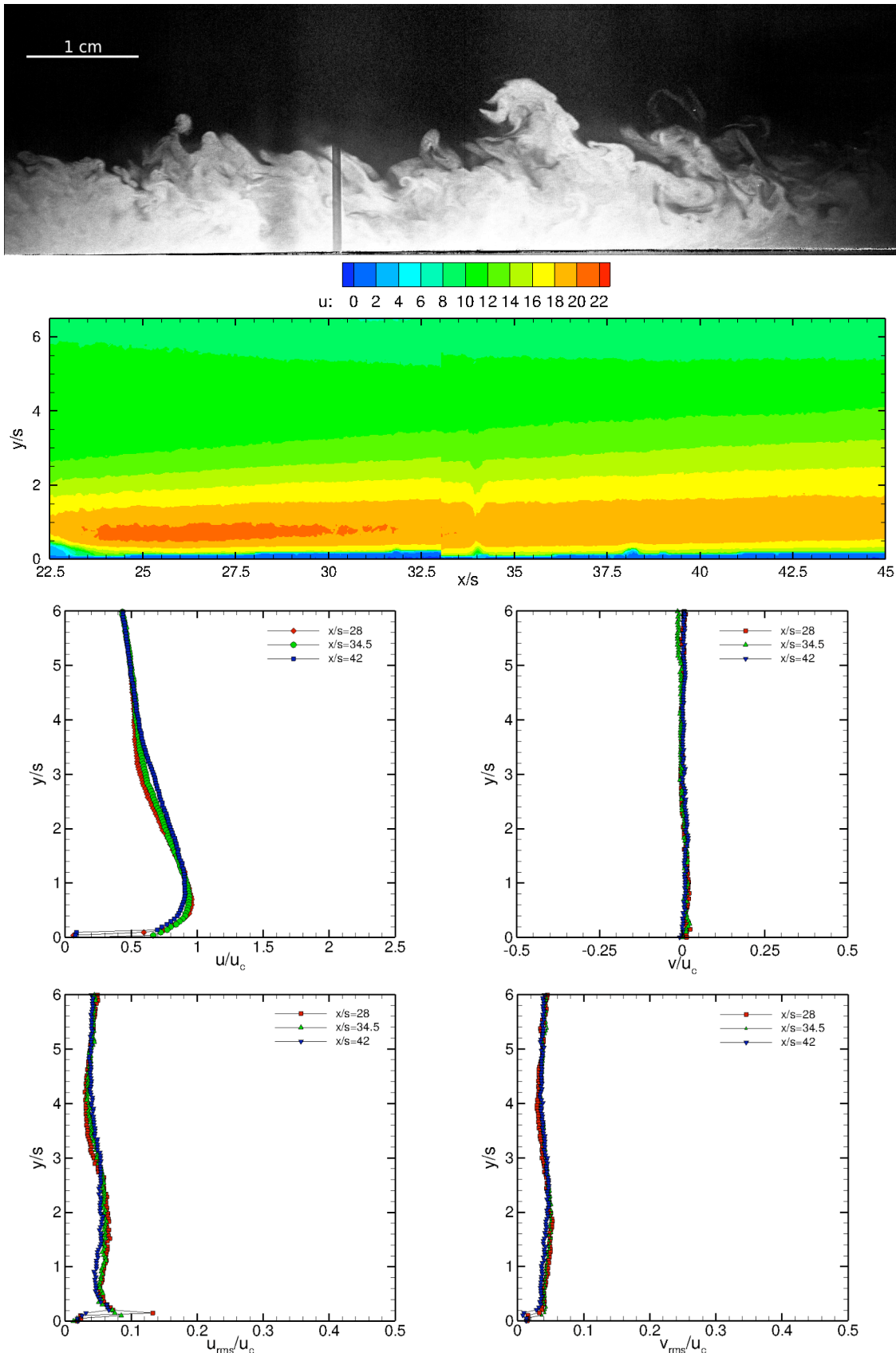


Figure A. 6. a) - f) VR = 2.0 Far Field

## Appendix B. Thermal Mixing

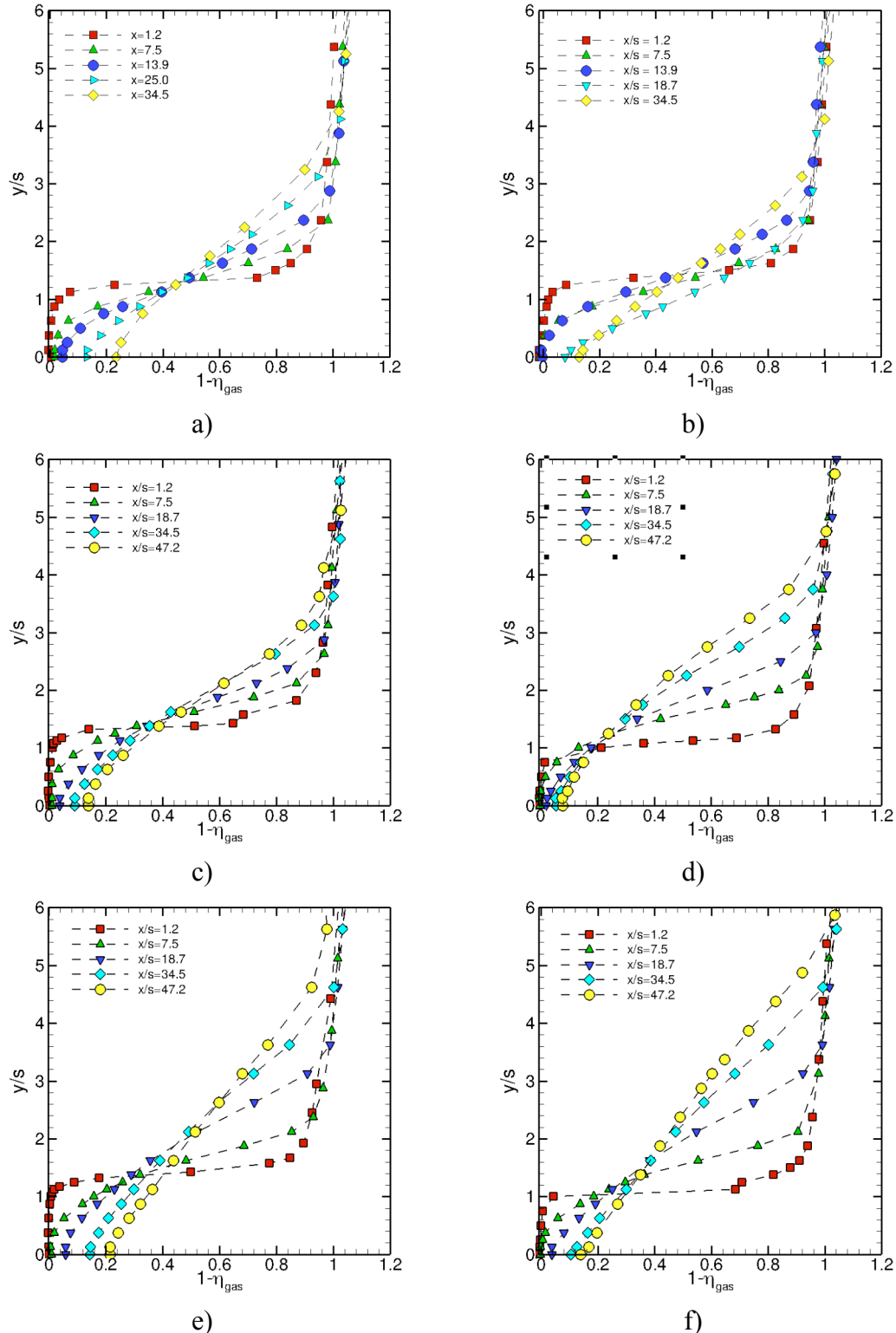


Figure B. 1. Non-dimensional thermal profiles a)  $m = 0.66$  adiabatic, b)  $m = 0.66$  non-adiabatic, c)  $m = 1.32$  adiabatic, d)  $m = 1.32$  non-adiabatic, e)  $m = 3.01$  adiabatic, f)  $m = 3.01$  non-adiabatic

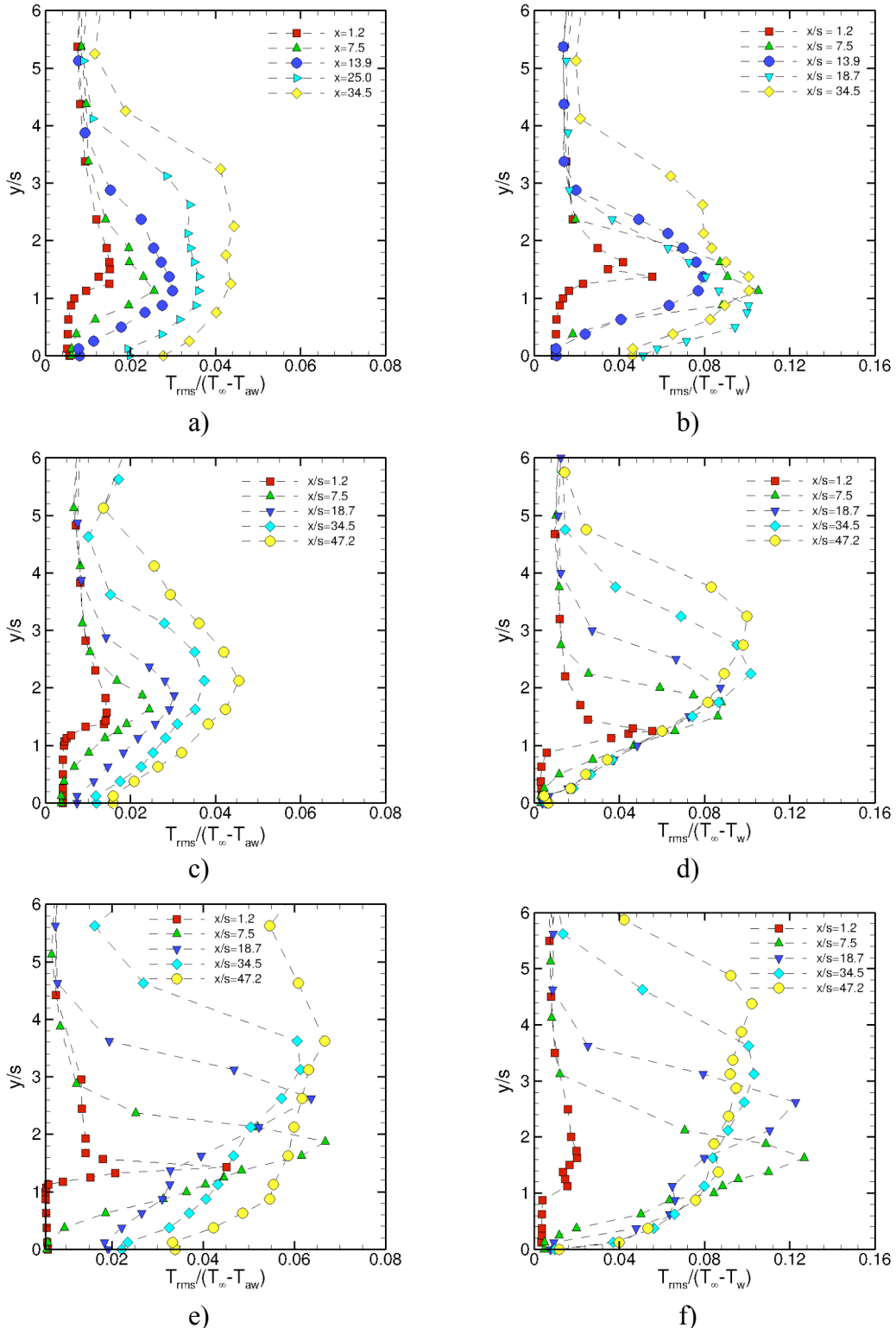


Figure B. 2. Non-dimensional thermal RMS profiles a)  $m = 0.66$  adiabatic,  
b)  $m = 0.66$  non-adiabatic, c)  $m = 1.32$  adiabatic, d)  $m = 1.32$  non-adiabatic,  
e)  $m = 3.01$  adiabatic, f)  $m = 3.01$  non-adiabatic

## Bibliography

---

<sup>1</sup> Sutton, G.P., "Rocket Propulsion Elements," John Wiley and Sons, New York, 5th edition, 1986

<sup>2</sup> Hill, P., Peterson, C., "Mechanics and Thermodynamics of Propulsion," Addison Wesley Longman, New York, 2<sup>nd</sup> edition, 1992

<sup>3</sup> Weighardt, K. "Hot Air Discharge for De-Icing," Air Material Command, AAF Trans. No. F-TS-919 RE, Dec. 1946

<sup>4</sup> Tribus, M., Klein, J., "Forced Convection from Non-Isothermal Surfaces," Heat Transfer, a Symposium, University of Michigan, Ann Arbor, 1953.

<sup>5</sup> Papell, S., Trout, A. "Experimental Investigation of Air Film Cooling Applied to an Adiabatic Wall by Means of an Axially Discharged Slot," NASA Technical Note D-9, August 1959

<sup>6</sup> Hatch, J.E., Papell, S., "Use of a Theoretical Flow Model to Correlate Data for Film Cooling or Heating an Adiabatic Wall by Tangential Injection of Gases of Different Fluid Properties," NASA Technical Note D-130, November 1959

<sup>7</sup> Papell, S., "Effect on Gaseous Film Cooling of Coolant Injection Through Angled Slots and Non-trivial Holes," NASA Technical Note D-299, September 1960

<sup>8</sup> Welsh, W.E., Review of Results of an Early Rocket Engine Film Cooling Investigation at the Jet Propulsion Laboratory, JPL Technical Report No. 32-58, March 1961

<sup>9</sup> Hartnett, J.P., Birkebak, R.C., Eckert, E.R.G., "Velocity Distributions, Temperature Distributions, Effectiveness and Heat Transfer for Air Injected Through a Tangential Slot Into a Turbulent Boundary Layer," Journal of Heat Transfer, pp. 293-306, August 1961

<sup>10</sup> Seban, R.A., Back, L.H., "Velocity and Temperature Profiles in a Wall Jet," Int. J. Heat Mass Transfer, Vol. 3, pp. 255-265, 1961

<sup>11</sup> Stollery, J.L, El-Ehwany, A.A.M, "A Note on the Use of a Boundary-Layer Model for Correlating Film-Cooling Data," Int. J. Heat Mass Transfer, Vol. 8, pp. 55-65, 1965

<sup>12</sup> Stollery, J. L., El-Ehwany, A. A. M., "Shorter Communication on the Use of a Boundary-Layer Model for Correlating Film Cooling Data," I Int. J. Heat Mass Transfer, Vol. 10, No. 1, pp. 101-105, 1967

<sup>13</sup> Goldstein, R.J., "Film Cooling," Advances in Heat Transfer, Vol. 7, Academic Press, New York, pp. 321-378, 1971

- 
- <sup>14</sup> Ballal, D.R., Lefebvre, A.H., "Film-Cooling Effectiveness in the Near-Slot Region," Journal of Heat Transfer, pp. 265-266, May 1973
- <sup>15</sup> Simon, F.F., "Jet Model for Film Cooling With Effect of Free-Stream and Coolant Turbulence," NASA Technical Paper 2655, October 1986
- <sup>16</sup> Marek, C.J., Tacina, R.R., "Effect of Free Stream Turbulence on Film Cooling," NASA Technical Note D-7958, 1975
- <sup>17</sup> Abramovich, G.N., "The Theory of Turbulent Jets," MIT Press, 1963
- <sup>18</sup> Cruz,C.A., Marshall, A.W., "Surface and Gas Measurements Along a Film-Cooled Wall," Journal of Thermophysics and Heat Transfer, Vol. 21, No. 1, January-March 2007
- <sup>19</sup> Bons, J.P, MacArthur, C.D., Rivir, R.B., "The Effect of High Freestream Turbulence on Film Cooling Effectiveness," Int. Gas Turbine and Aeroengine Technology Report, 1994
- <sup>20</sup> Taslim, M.E., Spring, S.D., Mehlman, B.P., "An Experimental Investigation of Film Cooling Effectiveness for Slots of various Exit Geometries," Journal of Thermophysics and Heat Transfer, Vol. 6, No. 2, April-June 1992
- <sup>21</sup> Burd, S.W., Simon, T.W., "Effects of Hole Length, Supply Plenum Geometry and Freestream Turbulence on film Cooling Performance," NASA /CR 2000-210226, August 2000
- <sup>22</sup> Gogineni, S.P., Pestian, D.J., Rivir, R.B., Goss, L.P., "PIV Measurements of Flat Plate Film Cooling Flows With High Free Stream Turbulence," AIAA 34<sup>th</sup> Aerospace Sciences Meeting and Exhibit, AIAA Paper 96-0617, January 1996
- <sup>23</sup> Sousa, J.M.M, Freek, C., Pereira, J.C.F., Merzkirch, W., "Visualization Study of Near-Wall Flow Using a DIC-PIV System," 8<sup>th</sup> International Symposium on Flow Visualization, 1998
- <sup>24</sup> Kays W.M., Crawford Michael E., Weigand Bernhard, "Convective Heat And Mass Transfer," 4th Ed., McGraw-Hill Education, United Kingdom, 2004
- <sup>25</sup> Spalart, P.R., "Direct Simulation of a Turbulent Boundary Layer up to  $Re_\theta = 1410$ ," Journal of Fluid Mechanics, Vol. 187, pp. 61-98, 1988
- <sup>26</sup> Fukushima, C., Aane, L., Westerweel, J., "Investigation of the Mixing Process in an Axisymmetric Turbulent Jet Using PIV and LIF, 10th International Symposium on Application of Laser Techniques to Fluid Mechanics, July 1999

---

<sup>27</sup> Peterson, S., "Structural Features of Jets-In-Crossflow for Film-Cooling Applications," 41<sup>st</sup> Aerospace Sciences Meeting and Exhibit, AIAA Paper 2003-303, January 2003

<sup>28</sup> Polanka, M.C., Cutbirth, J.M., Bogard, J.D., "Three Component Velocity Field Measurements in the Stagnation Region of a Film Cooled Turbine Vane," Journal of Turbomachinery, Vol. 124, pp.445-452, July 2002

<sup>29</sup> Kaehler, C.J., "The Significance of Coherent Flow Structures for the Turbulent Mixing in Wall-Bounded Flows," Dissertation zur Erlangung des Doktorgrades der Mathematisch-Naturwissenschaftlichen Fakultaten der Georg-August-Universitat zu Gottingen, 2004

<sup>30</sup> Baldauf, S., Schulz, A., Wittig, S., "High-Resolution Measurements of Local Heat Transfer From Discrete Hole Film Cooling," Journal of Turbomachinery, Vol. 123, pp. 749-757, October 2001

<sup>31</sup> Baldauf, S., Scheurlen, M., Schulz, A., Wittig, S., "Heat Flux Reduction From Film Cooling and Correlation of Heat Transfer Coefficients From Thermographic Measurements at Enginelike Conditions," Journal of Turbomachinery, Vol. 124, pp. 699-709, October 2002

<sup>32</sup> Saumweber, C., Schulz, A., Wittig, S., "Free-Stream Turbulence Effects on Film Cooling With Shaped Holes," Journal of Turbomachinery, Vol. 125, pp.65-73, January 2003

<sup>33</sup> Schulz, A., "Infrared Thermography as Applied to Film Cooling of Gas Turbine Components," Meas. Sci. Technology, Vol. 11, 2000

<sup>34</sup> Walters, D.K., Lylek, J.H., "A Detailed Analysis of Film Cooling Physics: Part I- Streamwise Injection With Cylindrical Holes," Journal of Turbomachinery, Vol. 122, pp. 102-112, January 2000

<sup>35</sup> McGovern, K.T., Lylek, J.H., A Detailed Analysis of Film Cooling Physics: Part II- Compound-Angle Injection With Cylindrical Holes," Journal of Turbomachinery, Vol. 122, pp. 113-121, January 2000

<sup>36</sup> Hyams, D.G., Lylek, J.H., "A Detailed Analysis of Film Cooling Physics: Part III- Streamwise Injection With Shaped Holes," Journal of Turbomachinery, Vol. 122, pp. 122-132, January 2000

<sup>37</sup> Brittingham, R.A., Lylek, J.H., "A Detailed Analysis of Film Cooling Physics: Part IV- Compound-Angle Injection With Shaped Holes," Journal of Turbomachinery, Vol. 122, pp. 133-145, January 2000

<sup>38</sup> Cruz, C. A., and Marshall, A. W., "Surface and Gas Phase Temperatures Near a Film Cooled Wall," AIAA Paper 2004-3654, 2004

---

<sup>39</sup> Raffel, M., Willert, C., and Kompenhans, J., “Particle Image Velocimetry,” 1st edition, Springer-Verlag, 1998

<sup>40</sup> Westerweel, J., “Fundamentals of Digital Particle Velocimetry,” Measurement Science Technology, Vol. 8, pp. 1379-1392, 1997

<sup>41</sup> Adrian, R.J., “Particle Imaging Techniques for Experimental Fluid Mechanics,” Annual Review in Fluid Mechanics, pp. 261-304, 1991

<sup>42</sup> Gaussorgues, G., “Infrared Thermography,” Chapman & Hall, 1994

<sup>43</sup> Siegel, R., Howell, J.R., “Thermal Radiation Heat Transfer,” 2<sup>nd</sup> edition, Hemisphere Publishing Corporation, New York, 1981

<sup>44</sup> Modest, Michael F., “Radiative Heat Transfer,” 2<sup>nd</sup> edition, Academic Press, San Diego, 2003

<sup>45</sup> Jakob, Mark, “Heat Transfer Vol. II,” John Wiley and Sons, New York, 1957

<sup>46</sup> Mills, K.C., “Recommended Values of Thermophysical Properties for Selected Commercial Alloys,” Woodhead Publishing, 2002

<sup>47</sup> Bevington, P. R., “Data Reduction and Error Analysis for the Physical Sciences,” New York: McGraw-Hill, pp. 58-64, 1969.